Contents lists available at ScienceDirect

Remote Sensing of Environment

journal homepage: www.elsevier.com

Review

Modelling the passive microwave signature from land surfaces: A review of recent results and application to the L-band SMOS & SMAP soil moisture retrieval algorithms

J.-P. Wigneron [a, *], T.J. Jackson [b], P. O'Neill [c], G. De Lannoy [d], P. de Rosnay [e], J.P. Walker [f], P. Ferrazzoli [g], V. Mironov [h], S. Bircher [i], J.P. Grant [j], M. Kurum [k], M. Schwank [l], J. Munoz-Sabater [e], N. Das [m], A. Royer [n], A. Al-Yaari [a], A. Al Bitar [i], R. Fernandez-Moran [a], H. Lawrence [e], A. Mialon [i], M. Parrens [i], P. Richaume [i], S. Delwart [o], Y. Kerr [i]

[a] *ISPA, INRA Bordeaux, France*
[b] *USDA, Beltsville, MD 20705, USA*
[c] *NASA/GSFC, Greenbelt, MD 20771, USA*
[d] *KULeuven, Heverlee, Belgium*
[e] *ECMWF, Reading, UK*
[f] *Monash University, Australia*
[g] *University of Rome Tor Vergata, Italy*
[h] *Kirenski Institute, Krasnoyarsk, Russia*
[i] *CESBIO, Toulouse, France*
[j] *Lund University, Lund, Sweden*
[k] *Mississippi State University, MS, USA*
[l] *Gamma Remote Sensing and WSL-Birmensdorf, Switzerland*
[m] *NASA/JPL, Pasadena, CA 91109, USA*
[n] *University of Sherbrook, Canada*
[o] *ESA ESRIN, Roma, Italy*

ARTICLE INFO

Article history:
Received 18 May 2016
Received in revised form 8 December 2016
Accepted 20 January 2017
Available online xxx

ABSTRACT

Two passive microwave missions are currently operating at L-band to monitor surface soil moisture (SM) over continental surfaces. The SMOS sensor, based on an innovative interferometric technology enabling multi-angular signatures of surfaces to be measured, was launched in November 2009. The SMAP sensor, based on a large mesh reflector 6 m in diameter providing a conically scanning antenna beam with a surface incidence angle of 40°, was launched in January of 2015. Over the last decade an intense scientific activity has focused on the development of the SM retrieval algorithms for the two missions. This activity has relied on many field (mainly tower-based) and airborne experimental campaigns, and since 2010–2011, on the SMOS and Aquarius space-borne L-band observations. It has relied too on the use of numerical, physical and semi-empirical models to simulate the microwave brightness temperature of natural scenes for a variety of scenarios in terms of system configurations (polarization, incidence angle) and soil, vegetation and climate conditions. Key components of the inversion models have been evaluated and new parameterizations of the effects of the surface temperature, soil roughness, soil permittivity, and vegetation extinction and scattering have been developed. Among others, global maps of select radiative transfer parameters have been estimated very recently. Based on this intense activity, improvements of the SMOS and SMAP SM inversion algorithms have been proposed. Some of them have already been implemented, whereas others are currently being investigated. In this paper, we present a review of the significant progress which has been made over the last decade in this field of research with a focus on L-band, and a discussion on possible applications to the SMOS and SMAP soil moisture retrieval approaches.

* Corresponding author.
Email address: wigneron@bordeaux.inra.fr (J.-JP.-P Wigneron)

http://dx.doi.org/10.1016/j.rse.2017.01.024
0034-4257/

1. Introduction

Passive microwave remote sensing at L-band (1–2 GHz) at the global scale with frequent revisit times is one of the most promising approaches to monitor soil moisture (SM) (Entekhabi et al., 2010; Jackson et al., 2010; Kerr et al., 2010). Three recent space missions use this technology: SMOS (launched in November 2009), Aquarius (launched in June 2011) and SMAP (launched in January 2015). The Soil Moisture and Ocean Salinity (SMOS) mission was the first space-borne mission dedicated to soil moisture mapping (Kerr et al., 2001; Kerr et al., 2010). Aquarius employed a set of three L-band radiometers and scatterometers, operating in a push-broom mode and covering a swath of about 300 km (Le Vine et al., 2010). Even though the primary mission objective of Aquarius was to provide global observations of sea surface salinity, it was also used for global SM (Bindlish et al., 2015). The Aquarius/SAC-D observatory was lost on June 7, 2015 due to a failure in the electronics supplying power to the observatory attitude control system. The most recent space-borne mission at L-band, the Soil Moisture Active Passive (SMAP) mission (Entekhabi et al., 2010), incorporated a radar and radiometer, both operating at the same incidence (observation) angle θ of 40°. The mission concept was to combine the complementary attributes of the radar observations (high spatial resolution but lower soil moisture sensitivity) and radiometer observations (higher soil moisture sensitivity but coarse spatial resolution), to retrieve SM at a spatial resolution of 9 km. Unfortunately, after successfully starting radar data acquisition in mid-April, the SMAP radar system stopped transmitting on July 7, 2015. The radiometer continues to operate as planned.

Several SM retrieval approaches have been developed in the context of these L-band space missions. The operational SMOS retrieval algorithm is based on the multi-angular and dual-polarization observing capabilities of the SMOS interferometric sensor: SM and vegetation optical depth tau at nadir (τ_{NAD}) (used to parameterize vegetation attenuation and emission) are retrieved simultaneously based on the SMOS multi-angular and dual-polarization observations of brightness temperatures TB (Wigneron et al., 2000). Specifically, the 2-Parameter (2-P) simultaneous retrievals of SM and optical depth at nadir (τ_{NAD}) are obtained from inversion of the L-MEB (L-band Microwave Emission of the Biosphere) model (Kerr et al., 2012; Kerr et al., 2016; Wigneron et al., 2007).

The forward model used, known as the τ–ω emission model, is a well-known zero-order solution of the radiative transfer equations, where optical depth τ and effective scattering albedo ω account for vegetation effects due to extinction and scattering, respectively (Mo et al., 1982; Wigneron et al., 1995). In addition, L-MEB includes a number of parameterizations to capture effects of vegetation structure and soil roughness on polarization and angular properties of L-band TB emitted from land surfaces.

The general retrieval approach proposed for SMAP was to use the active-channel (radar) for disaggregating the passive (radiometer) L-band TB to produce higher resolution data. The same algorithm would then be used for both the radiometer-only product and the disaggregated product. The current baseline algorithm is a version of the single-channel algorithm (SCA) (Jackson, 1993), which is also based on the τ–ω model. Unlike the algorithms for SMOS, only one polarization and one incidence angle of the SMAP TB is used to retrieve SM, while optical depth at nadir (τ_{NAD}) is not retrieved. Instead it is estimated from the linear relation $\tau_{NAD} = b \cdot VWC$ where values of the b-parameter are obtained from a land cover look up table and the vegetation water content (VWC) is estimated from a function which utilizes 13-year climatological values of the Normalized Difference Vegetation Index (NDVI) (O'Neill et al., 2015).

Both the SMOS and SMAP missions benefit from recent findings in microwave modelling. The SMOS mission relies on the L-MEB model (Wigneron et al., 2007) to produce time series of the Level 2 and Level 3 SM products since the beginning of 2010 (Al Bitar et al., 2016; Kerr et al., 2012; Kerr et al., 2016). These SM products have been evaluated against numerical modelling products and in-situ data from large SM networks included in the SMOS calibration/validation initiative (Al-Yaari et al., 2014; Kerr et al., 2016). Moreover, the L-MEB model was evaluated in a series of experimental campaigns based on field and airborne measurements (Bircher et al., 2012; Bircher et al., 2013; Fernandez-Moran et al., 2015; Martens et al., 2015; Merlin et al., 2009; Mialon et al., 2012; Panciera et al., 2009a; Pardé et al., 2011; Peischl et al., 2012; Peischl et al., 2014; Saleh et al., 2009; Schlenz et al., 2012; Yan et al., 2015). Numerical and physical models were used to develop new parameterizations of the soil roughness, soil permittivity, forests and low vegetation effects. Based on these activities some future improvements of the L-MEB model have been proposed and some of them have already been implemented in the SMOS operational algorithm.

The SMAP passive retrieval algorithm of Level 2 and 3 SM, as well as the Level 4 SM data assimilation product, rely on similar radiative transfer equations as SMOS and therefore, both missions mutually benefit from recent findings in this field of research, especially in terms of soil roughness parameterizations, modelling of the vegetation scattering effects linking vegetation indices and vegetation optical thickness etc. The core of this paper presents a review of the most significant recent modelling results obtained in the framework of the SMOS and SMAP L-band missions. Some recent and significant results obtained at higher frequencies will also be discussed, as there is continuity in the modelling between the L and higher frequency bands. In particular, recent results obtained at C- and X-bands from the Advanced Microwave Scanning Radiometer (AMSR-E and AMSR2) provide very useful insights for further development of the SMOS and SMAP algorithms. A discussion on the impact of recent TB modelling results on the SM retrieval accuracy and present perspectives is also provided.

2. Overview of the inversion algorithms used in SMOS and SMAP

Before we go into the details of the radiative transfer equations used in the SMAP and SMOS operational algorithms, we present in this section a brief overview of the main inversion algorithms used and/or evaluated in the framework of these two space-borne missions. One of the major differences in these different algorithms is the approach used to account for vegetation effects, through the parameterization or retrieval of vegetation optical depth (τ).

2.1. SMOS Level 2 and Level 3 operational algorithms

As presented in the introduction, in the SMOS operational algorithm, a 2-Parameter (2-P) retrieval of SM and optical depth ay nadir (τ_{NAD}) is performed based on the inversion of L-MEB, the forward model of the Level 2 and Level 3 operational algorithms. The L-MEB inversion is based on the minimization of a cost function using a generalized least-squares iterative algorithm which account for a priori information available for the retrieved parameters (Kerr et al., 2012). The inversion is carried out using multi-angular and dual polarization observations of brightness temperatures (TB). As the satellite moves along its track, a series of brightness temperatures emitted by the same location on earth is thus obtained for a range of distinct incidence angles (θ), which are available for the inversion. This range depends on the position of the pixel relative to the sub-satellite track.

The retrieval accuracy is best for "optimal" dates when the pixel is in the very central part of the Field of View (FOV) so that the range of incidence angles available for the inversion is maximum; typically ~ 0–55° (Wigneron et al., 2000).

If we assume that the optical depth (τ_{NAD}) varies relatively slowly over time, the value of τ retrieved on that "optimal" date can be used as the starting τ value for the SM and τ retrieval for the days before and the days after (days for which there is a reduced range of available incidence angle). This result is currently exploited to optimize SM retrievals in the L2 algorithm using so-called "current files" (Wigneron et al., 2000; Kerr et al., 2012). The Level 3 (L3) algorithm is very similar to the Level 2 (L2) algorithm except that it exploits the concept of "slowly varying optical depth" through a multi-orbit approach over a 7-day period. Over that period the retrieved values of optical depth are constrained using a temporal autocorrelation function (Al Bitar et al., 2016; Kerr et al., 2016). Note that there is a time sub-cycle of 18 days in the SMOS viewing configuration, meaning that the viewing geometry over a given pixel is almost the same at the time t and at the time t + 18 days. It is important to have in mind this specificity when analyzing the SMOS L2 and L3 products.

The large interest in the 2-P approach used in both the L2 and L3 SMOS algorithms is that no estimates of optical depth (τ) are required in the inversion process of SM. But, as noted above, if a priori estimates of τ are available, there is the option of using them as starting values and to constrain the inversion process (as done for the "current files" used in the SMOS L2 algorithm). The retrieved SMOS τ product is a "side-product" of SM and can be potentially very interesting to monitor vegetation, as it was demonstrated in studies based on the τ product computed from observations made at higher frequencies (Liu et al., 2013, 2015; Tian et al., 2016; Konings and Gentine, 2016b).

2.2. SMAP Level 2 operational algorithm

Currently, the Single Channel Algorithm (SCA), based on V-polarized TB data (SCA-V), is used as the SMAP baseline algorithm but the same algorithm can also be applied to H-polarized TB data (SCA-H).

The Single Channel Algorithm (SCA) is based on TB observations made at the one incidence angle of SMAP (θ = 40°) and at one given polarization. In SCA-V, TB_V data are converted to emissivity using a surrogate for the effective temperature of the emitting scene. The derived emissivity is corrected for vegetation and surface roughness to obtain the soil emissivity. Finally, a dielectric mixing model is used to obtain soil moisture SM from the soil dielectric constant using the Fresnel equations. The nadir optical depth (τ_{NAD}) is estimated from the vegetation water content (VWC) as,

$$\tau_{NAD} = bVWC \quad (1)$$

where b is a proportionality factor mainly depending on the vegetation structure (Jackson and Schmugge, 1991). The b values are obtained by means of a land cover look-up table and the baseline approach utilizes a set of land cover-based equations to estimate VWC from values of NDVI (O'Neill et al., 2015).

A total of four methods (SCA-H, SCA-V, DCA and LPRM) was considered in the SMAP Algorithm Theoretical Baseline Document (ATBD, O'Neill et al., 2015) and they are briefly presented in the following.

2.3. The dual channel algorithm (DCA)

The Dual Channel Algorithm (DCA) is an extension of the SCA and uses both H-polarized and V-polarized TB observations to simultaneously retrieve SM and τ(θ = 40°) (O'Neill et al., 2015). As in the SMOS algorithm, SM and τ(θ = 40°) are retrieved through the minimization of the root mean square difference between the simulated and observed TB data. The main difference between the SMOS and DCA algorithms is that TB data at θ = 40° are used for DCA, while multi-angular data are used for the 2-P L-MEB inversion.

2.4. Land parameter retrieval model (LPRM)

There are two steps in the LPRM approach. First, the vegetation optical depth is computed using an analytical solution based on the Microwave Polarization Difference Index (MPDI) and the observed surface emissivity (e_H and e_V), assuming that the values of the vegetation optical depth are the same for both polarizations. The MPDI index is calculated from the brightness temperature at H and V polarizations as follows (Meesters et al., 2005):

$$MPDI = \left(TB_V - TB_H\right) / \left(TB_V + TB_H\right) \quad (2)$$

Second, SM is retrieved using an optimization routine that minimizes the RMSE between the modelled (using the τ-ω emission model) and observed H-polarized brightness temperatures. As for SMOS and DCA, the vegetation optical depth is an additional retrieval result.

The LPRM was implemented on multi-frequency satellites such as AMSR-E (Owe et al., 2001, 2008; de Jeu et al., 2008), and more recently on SMOS (Van der Schalie et al., 2015; Van der Schalie et al., 2016). The effective temperature can be obtained from observations in the X-band V-polarized channel, as it is done for the AMSR-E products or from re-analysis or near real time data from weather prediction centres (Parinussa et al., 2011). All detailed equations of the LPRM approach are given in (Owe et al., 2001; Meesters et al., 2005; de Jeu et al., 2009).

2.5. Multi-orbit retrievals of soil moisture and optical depth (MT-DCA)

As done in the SMOS L3 algorithm, a method based on multi-orbit retrievals of (SM, τ) that takes advantage of the relatively slow temporal dynamics of early morning vegetation water content and combines a number of consecutive observations was proposed recently by Konings et al. (2016). Additionally, the algorithm retrieves a constant albedo. The algorithm was termed the multi-temporal dual channel algorithm (MT-DCA). MT-DCA has not yet been tested using SMOS or SMAP observations, but it has been evaluated using three years of L-band passive observations from the NASA Aquarius sensor. MT-DCA is mentioned here, to complete this brief overview of the main SM retrievals algorithms developed at L-band. A summary of the current modelling of the soil and vegetation effects within the SMOS and SMAP SM retrieval algorithms is given in Table 1. The different terms of the equations used in Table 1 are detailed in the following two sections for soil (Section 3) and vegetation (Section 4).

Table 1
Main components of the current version of the SMOS and SMAP L2 operational algorithms. Details on equations for soil and vegetation modelling are given in Sections 3 & 4.

Forward model/modelling component	L2 L3 SMOS mission (L-MEB)	L2 SMAP mission
Soil roughness modelling	H-Q-N modelling (Eq. (5)) H_R = 0.1 for low vegetation H_R = 0.3 for forests Q_R = 0; N_{RV} = 0, N_{RH} = 2	H-Q-N modelling (Eq. (5)) H_R = f(IGBP) Q_R = 0; N_R = 2
Modelling of the soil dielectric constant (ε_G)	Dobson before L2 V5.5 Mironov since L2 V5.5 (April 2012) ε_G = f(SM, T_G, % clay)	Mironov ε_G = f(SM, T_G, % clay)
Effective soil temperature	T_G = f(T_{soil_surf}, T_{soil_depth}) T_{soil_surf}, T_{soil_depth} from Layer 1 & 3 of ECMWF $C_T = (SM / W_0)^{b0}$ W_0, b_0 = f(soil type); default: W_0 = 0.3 m^3/m^3; b_0 = 0.3	T_G = f(T_{soil_surf}, T_{soil_depth}) T_{soil_surf}, T_{soil_depth} from Layer 1 & 2 of GEOS-5 FP-IT C_T = 0.246
Vegetation temperature	Skin temperature (ECMWF)	$T_C = T_G$, at 6:00 am LST
Vegetation modelling	τ-ω model (Mo et al., 1982)	τ-ω model (Mo et al., 1982)
Effective albedo	presently $\omega_V = \omega_H = \omega$ ω = 0 for low vegetation ω = 0.06–0.08 for forests	presently $\omega_V = \omega_H = \omega$ ω = f(IGBP)
Structural effects on τ	tt_P equations (Eq. (16)) default values: $tt_V = tt_H$ = 1	Presently $\tau_V = \tau_H$, at θ = 40°
Optical depth	τ_{NAD} results from 2-P retrievals of SM and τ_{NAD} τ_{NAD} = b′ LAI + b″([a])	τ_{NAD} = b VWC b = f(IGBP) VWC = f(NDVI, IGBP)

[a] Equation mainly used to initialize the inversion process and for specific inversion configurations (marginal impact on retrieval results but decrease in computation time).

2.6. Other algorithms

Various other L-band retrieval algorithms exist, including methods that circumvent the use of explicit radiative transfer calculations, such as those based on neural networks. However, in this paper we focus solely on algorithms that explicitly use radiative transfer processes to estimate soil moisture.

3. Soil radiometric modelling

This section presents the main principles of radiometric modelling of soil signatures in the passive microwave domain, the current models used in the SMOS and SMAP retrieval algorithms and some of the main improvements that have been made recently in this field, as related to the modelling of soil roughness effects, soil effective temperature and soil permittivity.

3.1. Background

3.1.1. General principles

The soil brightness temperature (TB_{GP}), where P represents polarization (P = V, Vertical or P = H, Horizontal), G represents "Ground" and θ is the incidence (observation) angle relative to nadir, can be written as (Ulaby et al., 1986):

$$TB_{GP}(\theta) = e_{GP}(\theta) \cdot T_G \quad (3)$$

where T_G is the effective soil temperature (assumed generally to be independent of polarization) and e_{GP} is the soil emissivity which can be computed from the soil reflectivity Γ_{GP} by (e.g. Peake, 1959):

$$e_{GP}(\theta) = 1 - \Gamma_{GP}(\theta) \quad (4)$$

In the case of smooth surfaces (no surface roughness), the smooth (specular) soil reflectivity Γ_{GP}^* can be computed from the Fresnel coefficients (Ulaby et al., 1986) as a function of the effective soil dielectric constant (ε_G) and the incidence angle (θ) relative to nadir. Several models have been developed to compute ε_G from volumetric SM (Dobson et al., 1985; Mironov et al., 2013a; Wang and Schmugge, 1980), using physically-based and semi-empirical modelling approaches. The main input parameters of these dielectric mixing models are soil moisture (SM, m^3/m^3), the effective soil temperature (T_G, K), and information on the soil properties, such as, texture (% of sand and clay), density, etc. For instance, the Mironov model (Mironov et al., 2013a) used in current SMOS retrievals requires as inputs SM, T_G and clay content (%).

To account for surface roughness, the approach above (i.e. Eqs. (3)–(4)) is employed with a modified surface reflectivity. Two main approaches are used to account for soil roughness effects:

(i) Physical models that relate radar scattering to thermal emission and then use Maxwell's equations to calculate the electric field scattered from the soil surface structure. Currently, the most widely used numerical methods for studying rough-surface scattering and emission are the method of moments (MoM; Huang et al., 2010) and numerical methods that utilize volume meshing such as the finite element method (FEM; Lawrence et al., 2011; Warnick and Chew, 2001). Analytical equations (Small Perturbation Method and the Kirchhoff Approximation, for instance) allowing wave scattering to be modelled from random rough surfaces and relying on simplifying assumptions have also been developed. The Small Slope Approximation (SSA; Broschat, 1993) and the Integral Equation Model (IEM; Fung, 1994; Shi et al., 2002) were successful in broadening the range of validity of these analytical approximations. In both the numerical and analytical approaches the values of the bistatic scattering coefficient are first computed from the scattered electric field by averaging over the ensemble of rough surfaces. Then the effective soil reflectivity needed in Eq. (4) is computed by integrating the bistatic scattering coefficients over the upper half-space (e.g. Peake, 1959). The roughness effects are usually characterized by a few geophysical parameters under the assumptions that the surface is isotropic (i.e. the roughness parameters are the same in every direction). These include the standard deviation of surface-heights (S_D), the autocorrelation function of surface heights (e.g. Gaussian, Exponential, etc.), and the associated values of the auto-correlation length (L_C).

(ii) Semi-empirical models relying on simple parametric equations derived from physical approaches. In this case, the values of the model parameters are calibrated (best-fit values) from data obtained from physical modelling (Lawrence et al., 2013; Schwank and Mätzler, 2006; Shi et al., 2002) or experiments (Mätzler et al., 2006; Montpetit et al., 2015; Wang et al., 1983; Wegmüller and Matzler, 1999; Wigneron et al., 2001; Wigneron et al., 2011). Empirical equations are generally used to make a link between the model 'best-fit' parameters and the classical geophysical parameters characterizing surface roughness (S_D, L_C, etc.). These model 'best-fit' parameters have to be considered as effective parameters as many assumptions have to be made to develop simplified analytical equations. For example, 3-Dimensional (3-D) spatial heterogeneities of soil moisture, structure and density are neglected; the roughness parameters are assumed to be the same

in every direction (isotropic assumption), etc. In particular, spatial heterogeneities in SM at the soil surface may lead to so-called dielectric "roughness" effects that combine with 'geometric' roughness effects (Mo and Schmugge, 1987; Panciera et al., 2009b; Schwank et al., 2010; Wigneron et al., 2001).

In summary, physical models allow the simulation of the soil emission for a large range of soil moisture and roughness conditions. However, considering the simplifications made in the representation of the soil medium, these methods can only be applied to 'ideal' surfaces with 'limited' imperfections in terms of heterogeneity and anisotropy. So, the applicability of these methods to simulate the emission from typically large footprints of radiometric observations from space is critical.

The weakness of semi-empirical approaches is that they are calibrated using limited data sets (most often from field observations) making them potentially site dependent. However, the parameters can be considered as effective parameters, accounting for many complex effects commonly found in natural environments (3-D soil spatial heterogeneities, volume scattering under dry soil conditions, effects of soil anisotropy) making these approaches more tractable for soil moisture retrievals. Currently, these methods are used in most of the algorithms developed for soil moisture retrievals from passive microwave observations.

3.1.2. Roughness modelling

To account for soil roughness effects, L-MEB has been based on the semi-empirical approach (referred here to as the HQN model), initially developed by Wang and Choudhury (1981) and utilizing two main parameters (H_{RP} and Q_R). The additional N_{RP} parameter was introduced in subsequent investigations (Escorihuela et al., 2007; Wigneron et al., 2001). The rough-surface reflectivity (Γ_{GP}) can be written as:

$$\Gamma_{GP}(\theta) = \left[\left(1 - Q_R(\theta)\right)\ \Gamma^*_{GP}(\theta) + Q_R(\theta)\ \Gamma^*_{GQ}(\theta)\right] \exp\left(-H_{RP}(\theta)\ \cos^{NR_P}(\theta)\right) \quad (5)$$

where $\Gamma_{GP}{}^*$ and $\Gamma_{GQ}{}^*$, (with P = H and Q = V or P = V and Q = H), is the specular reflectivity of a smooth surface and the roughness parameters H_{RP}, Q_R and N_{RP} can be described as follows:

- H_{RP} accounts for the intensity of the roughness effects (the emissivity generally increases as H_{RP} increases, for increasing soil roughness). As the dependence of H_{RP} on polarization P = V or P = H is often accounted for using the N_{RP} parameter, H_{RP} will be referred to as H_R in the following. More generally, in this review the dependence on polarization of the roughness parameters will be accounted only through the N_{RP} parameters (p = V or p = H).
- Q_R is a polarization mixing parameter (the difference between the values of emissivity at horizontal and vertical polarizations decreases as Q_R increases).
- N_{RP} was introduced to better account for multi-angular and dual-polarization measurements. In the initial study of Wang and Choudhury (1981), N_{RP} (P = V, H) was set equal to 2.

Several studies have investigated the link between these three roughness parameters and the geophysical parameters characterizing the surface roughness, in terms of standard deviation (S_D), auto-correlation length (L_C), autocorrelation function (Gaussian, exponential, …), etc. These surface roughness characteristics are measured for example with an automated laser profilometer or a needle board, with a sampling interval varying between 0.2 cm and 1 cm along a 1-, 2- or 3-m transect over each field (usually, ten measurements at least are made in two directions, i.e., parallel and perpendicular to the field rows).

However, it remains difficult to draw general conclusions from these initial studies, for several reasons. The main reasons are:

(i) The four parameters (H_R, Q_R, N_{RV} and N_{RH}) are not independent. Decoupling their effects requires very large data sets, obtained for a large range of configurations in terms of surface conditions (soil moisture, roughness, temperature, etc.) and of observation systems (polarization, incidence angle, frequency, …), which are very rarely available.

(ii) There is a large uncertainty in the estimation of the geophysical parameters characterizing surface roughness from field measurements. Moreover, the characterization which is made in terms of values of S_D, L_C and auto-correlation function is not sufficient (or appropriate) to characterize features of surface roughness in natural and agricultural environments considering, 2-Dimensional heterogeneities at field scale (Oh and Kay, 1998), separate consideration of the 'micro-scale' and 'macro-scale' roughness (Gao et al., 2013), row effects (Völksch et al., 2015), etc.

(iii) The conclusions differ depending on whether the focus is on the accuracy in the TB simulations or in the SM retrievals (Lawrence et al., 2013).

In support of the above comments, a brief review of these studies is provided subsequently. Most of the published studies specify or assume that the value of Q_R increases with frequency, from a value close to 0.0 at L-band, ~ 0.1 at C-band, to 0.2–0.3 at X-band (Wang et al., 1983). Note that non-zero values of Q_R should be used to simulate specific effects (emissivity may decrease as roughness increases) as revealed by Shi et al. (2002) at V polarization for large incidence angles. In terms of SM retrievals, the Q_R parameter is generally assumed to be zero at L-band (Wang et al., 1983). In the latter case, Eq. (5) can be simplified to:

$$\Gamma_{GP}(\theta) = \Gamma^*_{GP}(\theta) \cdot \exp\left(-H_R(\theta) \cdot \cos^{N_{RP}}(\theta)\right) \quad (6)$$

In the literature, contrary to Q_R, the H_R parameter is found to be a key parameter to account for roughness effects. Choudhury et al. (1979) developed the formulation $H_R = (2 \cdot k \cdot S_D)^2$, where $k = 2\pi/\lambda$ is the wavenumber at wavelength λ, which has been widely used in the literature over a large frequency range (Kerr and Njoku, 1990) especially to model the coherent component of the soil reflectivity (Mo and Schmugge, 1987; Shi et al., 2002). However, several studies (Choudhury et al., 1979; Mo and Schmugge, 1987; Wigneron et al., 2001) found that this latter formulation may lead to an overestimation of the roughness effects for medium and very rough soil conditions. Both Mo and Schmugge (1987) and Wigneron et al. (2001) found the best estimates of the value of H_R were made with the slope parameter $m = S_D/L_C$ through a power-law relationship. Several studies (Escorihuela et al., 2007; Mo and Schmugge, 1987; Schneeberger et al., 2004; Wigneron et al., 2001) also noted a sensitivity of H_R to SM with H_R increasing for dry soil conditions. This sensitivity was interpreted as an effect of the "dielectric roughness" which increases as the soil gets drier due to SM spatial heterogeneities as opposed to "geometric roughness", parameterized by S_D and L_C. Wigneron et al. (2001) noted that these "dielectric roughness" effects could be enhanced by the larger thermal sampling depth over dry soils. Early

work noted that the frequency dependence of H_R is generally considered as low (Wang et al., 1983).

As for the N_{RP} parameter, initial studies considered a $\cos^2(\theta)$ dependence in Eq. (5) (Choudhury et al., 1979; Wang and Choudhury, 1981). However, Wang et al. (1983) found this dependence was "much too strong" and proposed to set $N_R = 0$. Since then, the values $N_R = -1$, 0 or 1 have been widely used in the literature (Bircher et al., 2012; de Jeu et al., 2009; Njoku and Chan, 2006; Peischl et al., 2012; Schlenz et al., 2012; Wigneron et al., 2001). The study by Escorihuela et al. (2007) was one of the first studies showing that the values of N_R for both H and V polarizations should not necessarily be the same. Based on long term measurements over a relatively smooth field ($S_D \sim 1$ cm, SMOSREX experiment, de Rosnay et al., 2006), Escorihuela et al. (2007) proposed to use $N_{RH} \approx 1$ and $N_{RV} \approx -1$, in agreement with Wigneron et al. (2007) who found values of N_{RP} varying between ~− 1 and + 1 over crop fields. Similarly, Bircher et al. (2012, 2013) found that best TB simulations and SM retrievals were obtained using $N_{RV} = -1$ and $N_{RH} = 0$ over a variety of crops fields in Denmark. Default values $N_{RV} = 0$ and $N_{RH} = 2$ are used in the SMOS algorithm. Note that there is a limited interest in using the N_{RP} parameter for sensors with mono-angular observations (such as AMSR-E and SMAP), as the term $\cos^{NRP}(\theta)$ in Eq. (5) will only be a scaling factor modulating the value of H_R.

3.2. Recent advances in roughness modelling

3.2.1. Results from observations made at field scale

The L-MEB soil roughness parameters were first established in the late 2000s (Table 1). Since then, several studies have been published providing new insights into modelling of the roughness effects. The most significant results are presented in the following.

It is known that microwave emission depth decreases with increasing SM. For instance, Escorihuela et al. (2010) showed that the soil moisture sampling depth specified in TB simulations has a strong impact on the calibrated values of soil roughness parameters. They found that the best correlation was obtained between TB and SM when measured over the 0–2 cm surface layer; for wet soils, the best correlation was between TB and SM measured over the 0–1 cm surface layer. Accounting for these effects, a low dependency of the roughness parameter H_R on SM was found. These results were confirmed by two further studies (Lawrence et al., 2013; Wigneron et al., 2011).

Based on the experimental PORTOS-1993 data set, Wigneron et al. (2011) developed an empirical relationship between H_R and S_D (Fig. 1), showing a saturation of H_R (towards values close to 1.1–1.2) when S_D exceed ~ 50–60 mm (corresponding to the extreme roughness conditions of freshly plowed soils):

$$H_R = \left(\frac{0.9437\, S_D}{0.8865\, S_D + 2.2913} \right)^6 \qquad (7)$$

As presented later, this relationship has been validated over a large frequency range (1.4–90 GHz) by Montpetit et al. (2015), confirming the rather low sensitivity of the value of H_R on the frequency band of the radiometric observations, as first noted by Wang et al. (1983). Based on simulated L-band TB data, Lawrence et al. (2013) found that best results for TB were obtained using a linear relationship between H_R and the parameter Z_S (cm) defined as $Z_S = S_D^2 / L_C$ as shown in Fig. 2 (top left panel). This relationship is in good agreement with Eq. (7), showing saturation of H_R close to values of ~ 1.2 for rough soil conditions ($Z_S > 1.2$ cm). Zribi and Dechambre (2003) were the first to explore the parameterization of soil roughness effects

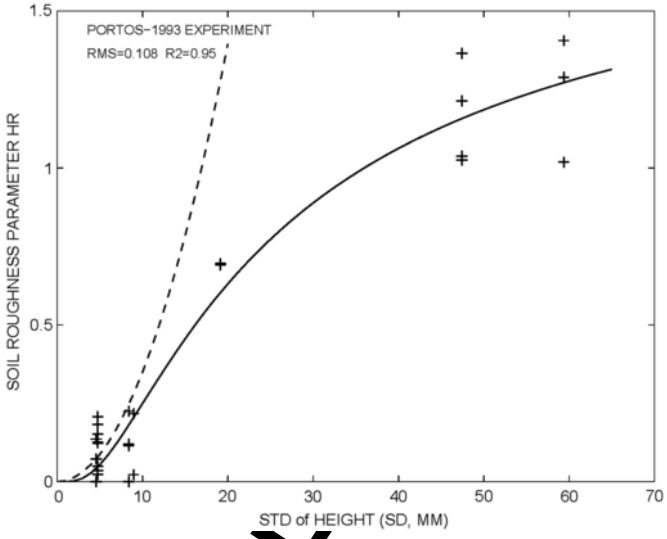

Fig. 1. Retrieved values of the roughness parameter HR as a function of the standard deviation of the surface height (S_D, mm) at L-band. Best fit relation given by Wigneron et al. (2011) (——) and the relation of Choudhury et al. (1979) (- - -) are included (adapted from Wigneron et al., 2011).

using the Z_S parameter in the active microwave domain. It seems there is a convergence of results, in both the passive and active domains, showing the interest of the parameter Z_S to parameterize the roughness effects.

In the initial L-MEB study, Wigneron et al. (2007) found typical values of H_R over crop fields varying between ~ 0.1–0.2 for soybean and wheat, to ~ 0.7 for corn fields. Since then, many studies have evaluated the calibration of H_R from tower-based or airborne observations. For instance, $H_R \sim 0.8$ over an oilseed rape canopy (Schlenz et al., 2012); H_R varying between 0.7 and 1.7 over a variety of forest and agricultural sites in the Southwestern region of France (Pardé et al., 2011); $H_R \sim 0.4$ over grass and open woodland, and ~ 1 over crops in the Goulburn River catchment, Australia (Saleh et al., 2009); $H_R \sim 0.35$ over natural shrubs in the Mediterranean region (Cano et al., 2010), etc.

There is a good general agreement between calibrated values of H_R based on experimental data and modelled values of H_R using Eq. (7). For instance, the retrieved values of H_R obtained over bare soils during the third Soil Moisture Active Passive Experiment (SMAPEx-3; Panciera et al., 2014) airborne campaign, in south-eastern Australia match very well the model in Eq. (7), especially for $S_D > 40$ mm (Gao et al., 2013). Good results were obtained too using the modelling Eq. (7) by Bircher et al. (2012, 2013) based on data from the HOBE airborne campaign in Western Denmark. However, without clear explanations higher values of H_R have been obtained from some experimental observations, especially from airborne campaigns (Panciera et al., 2009a; Pardé et al., 2011; Peischl et al., 2012). In addition, the use of a SM dependent parameter $H_R(SM)$ has been tested in the above-mentioned studies, but no clear general conclusion could be drawn on the impact of SM retrieval performance: Sometimes improvements are found considering $H_R(SM)$, sometimes not. For instance, based on data from the SMAP Validation Experiment 2012 conducted in Canada, Martens et al. (2015) found that the linear dependence of H_R on SM cannot be generalized and that it is mainly valid for sandy soils.

As for the N_{RH} and N_{RV} parameters, Lawrence et al. (2013) obtained results over a large range of roughness conditions. They extended the results obtained by Escorihuela et al. (2007) for rather smooth soil conditions, showing the difference $\Delta N_R = N_{RH} - N_{RV}$ de-

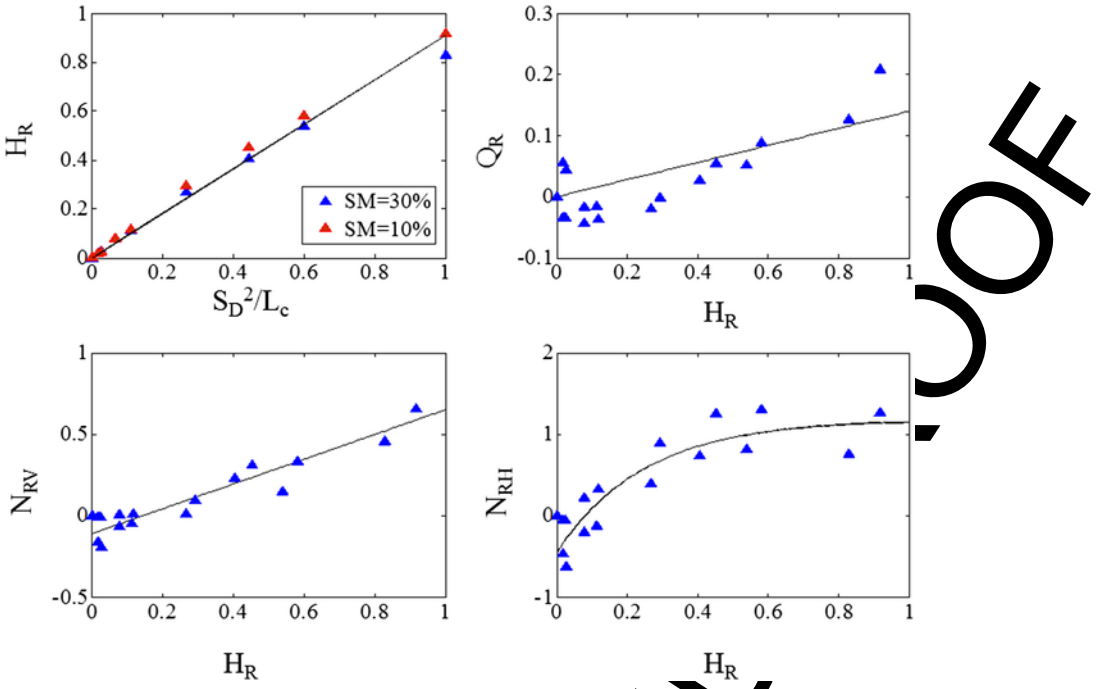

Fig. 2. Retrieved values of the roughness parameters: (Top left) H_R as a function of the parameter $Zs = S_D^2/L_C$ for two values of soil moisture (SM = 0.10 m^3/m^3 and SM = 0.30 m^3/m^3), (Top right) Q_R, (Bottom right) N_{RV}, and (Bottom left) N_{RH} as a function of retrieved H_R (adapted from Lawrence et al., 2013).

creased from a value ~ 2 for smooth surfaces to ~ 1–1.5 for rough soils, in agreement with experimental results by Mialon et al. (2012). For TB simulations, Lawrence et al. (2013) proposed a model where H_R is computed from Z_S, while Q_R, N_{RV} and N_{RH} are computed from H_R (Fig. 2). The values of N_{RV} and N_{RH} increase with increasing values of H_R; their values varying between − 0.5 and 1. However, they found that setting $N_{RV} = N_{RH}$ led to a simplified model with good performance in terms of both TB modelling and SM retrievals. Lawrence et al. (2013) also found that the values of Q_R increase for increasing soil roughness (up to ~ 0.2–0.4) but its value can be set to $Q_R = 0.0$ for smooth or medium roughness conditions. They also found that assuming $Q_R = 0$ did not degrade model accuracy, both in terms of TB forward modelling and SM retrievals. Note that for these simulations assuming homogeneous soil moisture conditions, the dependence of the computed roughness parameters on SM was found to be very low (Fig. 2, top left panel).

At the scale of satellite passive microwave observations, the above results cannot be easily applied to estimate the values of the model roughness parameters required to simulate TB of large footprints. It is likely that the calibrated values of the roughness parameters over large areas also include topographic slope distributions (undulating, gently rolling to strongly rolling) (Wang et al., 2015) or surface effects related to litter especially over grasslands and forests (Grant et al., 2008; Saleh et al., 2006). Note that the topographic effects have been analyzed in several studies (e.g. Talone et al., 2007; Monerris et al., 2008; Utku and Le Vine, 2014) and that they are currently flagged as described in (Mialon et al., 2008) in the SMOS SM products.

However, a better understanding of the relationship between the roughness model parameters and the geophysical parameters characterizing the "geometric roughness" (such as S_D and L_C) could be useful in the interpretation of the radiometric signatures over agricultural areas from space-borne sensors as found by Patton and Hornbuckle (2013).

3.2.2. *Results obtained from space-borne observations*

In both the SMOS and SMAP Level 2 algorithms, the effects of soil roughness are taken into account using the HQN model given by Eq. (5). The current SMOS algorithm (V620) considers the parameters as default values: $H_R = 0.1$ over low vegetation and $H_R = 0.3$ over forests and $Q_R = 0$, $N_{RV} = 0$, $N_{RH} = 2$ over both low vegetation and forests. In the current SMAP SM algorithm, the soil reflectivity is modelled too as a function of the Fresnel reflectivity $\Gamma^*_{GP}(\theta)$ from Eq. (5) considering $N_R = 2$ (as mentioned previously the $\cos^{NRP}(\theta)$ term in Eq. (5) is only a scaling factor of H_R for a mono-angular sensor such as SMAP and it is dropped to avoid overcorrecting for roughness). H_R is tabulated as a function of land cover types for the current SMAP Level 2 algorithms using the International Geosphere-Biosphere Programme (IGBP) classification scheme (Channan et al., 2014) (Table 2). Spatially and temporally variable estimates of global H_R have been estimated and may be used in future SMAP Level 2 and 3 products (personal communication Steven Chan). The SMAP Level 4 soil moisture product (L4_SM) already uses spatially and temporally variable H_R values, which are estimated along with other key radiative transfer parameters using Bayesian inference and historical SMOS time series (De Lannoy et al., 2013; De Lannoy et al., 2014). These parameter inputs are provided as part of the L4_SM data product (Entekhabi et al., 2014).

Parrens et al. (2016) also estimated maps of H_R using SMOS data, assuming that $N_{RV} = N_{RH} = -1$ and $Q_R = 0.0$. They obtained values (Table 2, Fig. 3) in good agreement with the literature: lower values (~ 0.15) of H_R were found over shrubs, bare ground, and desert; intermediate values (~ 0.2–0.25) over cultivation, tundra and wooded grassland, and higher values (0.30–0.40) over forests. Currently, the H_R values used in the SMAP Level 2 algorithm (they range between ~ 0.11 for croplands to 0.16 for forests) have a narrower range than the ones used by the SMOS algorithm (ranging currently from 0.1 to 0.3) and the ones found in the global studies by De Lannoy et al. (2013, 2014) and Parrens et al. (2016).

Table 2
Roughness parameter H_R by IGBP class considered in the SMOS Level 2 algorithm, (Kerr et al., 2014; Kerr et al., 2012), SMAP Level 2 algorithm (O'Neill et al., 2015) and computed from the SMOS observations at global scale over 2011 (Parrens et al., 2016).

Land cover type	SMOS[a] (default)	SMAP[a]	Parrens et al. (2016)[b]
Evergreen needleleaf forests	0.30	0.160	0.35
Evergreen broadleaf forests	0.30	0.160	0.46
Deciduous needleleaf forests	0.30	0.160	0.43
Deciduous broadleaf forests	0.30	0.160	0.45
Mixed forests	0.30	0.160	0.41
Closed shrublands	0.10	0.110	0.26
Open shrublands	0.10	0.110	0.17
Woody savannas	0.10	0.125	0.35
Savannas	0.10	0.156	0.23
Grasslands	0.10	0.156	0.13
Permanent wetlands	0.10	–	0.20
Croplands	0.10	0.108	0.17
Urban and built-up lands	0.10	0.000	0.19
Crop-land/natural vegetation mosaics	0.10	0.130	0.22
Barren or sparsely vegetated	0.10	0.150	0.02

[a] $N_{RV} = 0$ and $N_{RH} = 2$ in the SMOS algorithm; $N_{RV} = N_{RH} = 2$ in the SMAP algorithm.

[b] $N_{RV} = N_{RH} = -1$.

3.2.3. *Results obtained over a wide frequency range*

Two main studies considered a large range of system configurations in terms of frequency (including the L-band and the frequency range of AMSRE, i.e. 6.9–89 GHz), incidence angle and polarization for the simulation of soil roughness effects. First, the model of Wegmüller and Matzler (1999) is widely used in that field. It is based on the results of Mo and Schmugge (1987) and considers four main parameters to model soil reflectivity at H-polarization (Γ_{GH}), and then derive soil reflectivity at V-polarization from Γ_{GH}.

Second, Montpetit et al. (2015) evaluated the HQN model. They computed H_R using an equation similar to Eq. (7) as a function of three parameters a_1, a_2, and a_3:

$$H_R = \left(\frac{a_1 S_D}{a_2 S_D + a_3} \right)^{6.}$$

Based on the PORTOS-93 data set, Montpetit et al. (2015) found the HQN model to be very accurate for simulating the soil roughness effects, using the same values of H_R (computed from Eq. (8) using $a_1 = 0.887$, $a_2 = 0.796$ and $a_3 = 3.517$), $Q_R = 0.075$, $N_{RV} = 1.5$ and $N_{RH} = 0.13$, over the whole 1.4–90 GHz frequency range. The model by Wegmüller and Matzler (1999) was also found to be accurate in simulating the rough surface emission provided specific values of the roughness model parameters were calibrated separately for each frequency band. Using this model, the sensitivity study by Montpetit et al. (2015) shows (Fig. 4) that there is a decrease in sensitivity of TB to SM for increasing roughness conditions and that there is an increasing sensitivity of TB to roughness for wet conditions (at H-polarization only).

Two further findings are more surprising: the authors found the sensitivity of TB to both SM and roughness to be almost the same over a large frequency range (1.4–23.8 GHz); the sensitivity to roughness at L-band being slightly higher for wet conditions. Even though there is not a consensus on these results, they are in good agreement with observations made by Wang et al. (1983) at 1.4, 5 and 10.7 GHz. So, based on the study of Montpetit et al. (2015) and in comparison to passive C- and X-band sensors, the main asset of L-band radiometers applied to SM estimation would be (i) the higher penetration capabilities through vegetation. For instance, Al-Yaari et al. (2014) found that, for high Leaf Area Index (LAI) values, improved performances in SM retrievals were obtained from L-band SMOS observations in comparison to C-band AMSR-E observations; (ii) the larger soil sampling depths (~ 0–3 cm at L-band, and ~ 0–1 cm at C- and X-bands; Raju et al., 1995); and (iii) the lower atmospheric effects.

3.3. *Soil effective temperature*

Effective soil temperature (T_G) is used to simulate upwelling brightness temperature TB_{GP} (Eq. (3)) of a soil considering vertical temperature and moisture gradients. An incongruity can be noted here: originally Eq. (3) was written for a homogeneous soil medium (with temperature and SM independent of depth), while the concept of effective temperature was developed to account for temperature and moisture gradients. So the use of an effective temperature concept in Eq. (3) leads necessarily to consider e_{GP} as the effective emissivity of the ground.

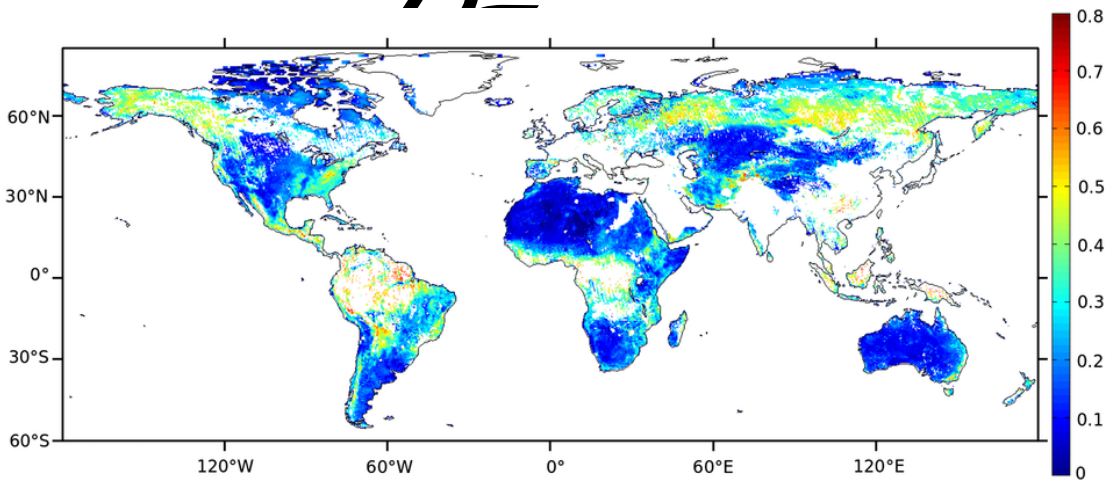

Fig. 3. Global map of the roughness parameter H_R retrieved from the SMOS observations at L-band (Parrens et al., 2016).

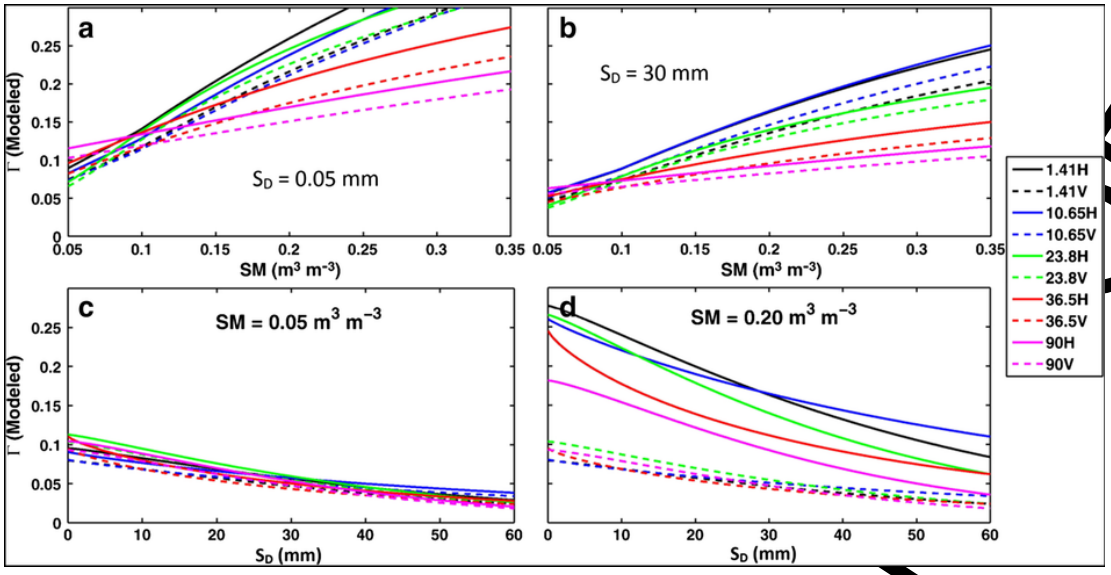

Fig. 4. Modelled reflectivity at H-Pol (solid line) and V-Pol (dashed line) at 1.41 (black), 10.65 (blue), 23.8 (green), 36.5 (red) and 90 GHz (magenta) as a function of a) soil moisture (SM) for (a) a low (S_D = 0.05 mm), or (b) high soil surface roughness (S_D = 30 mm), and as a function of S_D (c) for a low (SM = 0.05 m^3/m^3) or (d) high soil moisture value (SM = 0.20 m^3/m^3; θ = 20° and soil T_G = 300 K, Montpetit et al., 2015). (For interpretation of the references to colour in this figure legend, the reader is referred to the web version of this article.)

T_G is generally considered to be expressed as (Ulaby et al. 1986):

$$T_G = \int_0^{\infty} TS(z)\ \alpha(z) \exp\left[-\int_0^{z} \alpha(z')\, dz'\right] dz \quad (9)$$

where $T_S(z)$ is the soil temperature at depth z, and the power attenuation coefficient α(z) is related to the complex soil dielectric constant $\varepsilon_G = \varepsilon_G' + i\cdot\varepsilon_G''$ and the observation wavelength λ as (Schwank et al., 2005):

$$\alpha(z) = (4\pi/\lambda)\cdot \mathrm{Im}\left(\sqrt{\varepsilon_G(z)}\right) \quad (10)$$

where Im() represents the imaginary part.

Based on this formulation and experimental data, Choudhury et al. (1982) developed a simple parameterization of the effective soil temperature T_G (Choudhury scheme):

$$T_G = T_{soil\_depth} + C_T\ \left(T_{soil\_surf} - T_{soil\_depth}\right) \quad (11)$$

where T_{soil_depth} is the deep soil temperature (50 to 100 cm); T_{soil_surf} is the surface temperature (0 to 5 cm) and the C_T parameter was computed as a function of the frequency band (C_T = 0.246 at L band).

This equation was refined by Wigneron et al. (2001) by accounting for the dependence of the parameter C_T on soil moisture ($C_T = (SM/W_0)^{b0}$, with $C_T \leq 1$ and where W_0 and b_0 are fitting parameters, Wigneron scheme) and then by Holmes et al. (2006) as function of the soil dielectric constant ($C_T = (\varepsilon_G''/\varepsilon_G')/\varepsilon_0)^{b0}$, where ε_0 and b_0 are fitting parameters; Holmes scheme). In a second step, Wigneron et al. (2008) improved the Wigneron scheme $C_T = (SM / W_0)^{b0}$ by accounting for the dependence of the W_0 and b_0 parameters on soil texture. This parameterization is currently implemented in the SMOS algorithm using the L-MEB default parameters W_0 = 0.3 m^3/m^3 and b_0 = 0.3. T_{soil_surf} and T_{soil_depth} are estimated from, respectively, ECMWF (European Centre for Medium-Range Weather Forecasts) Level 1 (1–7 cm) and Level 3 (28–100 cm) soil temperature data. The SMAP algorithm is based on Eq. (11) using C_T = 0.246 (Choudhury et al., 1982) and T_{soil_surf} and T_{soil_depth} are estimated by the GSFC GMAO GEOS5 forecasted soil temperatures in the first layer (0–10 cm) and second layer (10–20 cm), respectively (Table 1). Recently, a new approach to compute C_T was derived from Eq. (9) for a two layer soil system by Lv et al. (2014) (Lv scheme). It accounts for the sampling depth (Δx) of the microwave radiation:

$$C_T = 1 - \exp\left(-\Delta x\ 4\pi/\lambda\ \left(\epsilon_G''/2\sqrt{\epsilon_G'}\right)\right) \quad (12)$$

An evaluation made over the Maqu site (Tibetan Plateau) of the four schemes (Choudhury, Lv, Holmes, and Wigneron) by Lv et al. (2014) found both the Lv and Wigneron schemes performed similarly (RMSE ~ 1.8–2.5 K) and better than both the Holmes scheme (RMSE ~ 3.5 K) and the Choudhury scheme (RMSE ~ 4.0 K). Note that, presently, most of the studies investigating the computation of T_G have been based on in-situ experimental data and a long term analysis based on satellite observations has still to be made to evaluate more extensively the different modelling schemes described above.

3.4. Dielectric models of moist soils

The microwave dielectric modelling of moist soils is an essential part of the retrieval algorithms in radar and radiometry remote sensing (Mätzler et al., 2006). Simple soil dielectric models can be applied in iterative retrieval algorithms to account for the dependence of the relative permittivity on solid soil phases, liquid soil water content, soil temperature and wave frequency. The most popular models used in the microwave remote sensing community are the ones developed by Wang and Schmugge (1980), Dobson et al. (1985), and Mironov et al. (2004). As compared with the model of Dobson et al. (1985),

the basic feature of the dielectric model of Mironov et al. (2004) consists of the fact that the latter distinguishes between bound and free soil water by considering the dielectric relaxation spectrum parameters for each type of soil water (bound and free), using the measured dielectric spectra of moist soil samples at fixed texture and temperature. This model is known in the literature as the Generalized Refractive Mixing Dielectric Model (GRMDM). On the basis of GRMDM, the dependence of the soil permittivity spectra on soil texture at a fixed temperature (Mironov et al., 2009) and on soil temperature at a given soil texture (Mironov & Fomin, 2009b), were established. The approaches of (Mironov & Fomin, 2009b; Mironov et al., 2009) were combined to compute the temperature and moisture dependent GRMDM in the case of mineral thawed soils (Mironov & Fomin, 2009a). Later, an engineering GRMDM dielectric model designed for the SMOS retrieval algorithm was developed (Mironov et al., 2013a): simplified and specific equations were developed at L-band and a larger validation data set was used. The methodology of GRMDM was also extended to take into consideration frozen soils and the thawed/frozen transitions of moist soils in the cases of both an organic-rich soil (Mironov et al., 2010) and a mineral soil (Mironov & Lukin, 2011). Later on, in the frame of the GRMDM methodology, an approach allowing different types of dielectric relaxations (dipole and ionic) in different soil water components to be distinguished was developed (Mironov et al., 2013b; Mironov et al., 2013c), leading to the development of dielectric models predicting the soil permittivity of thawed and frozen organic rich soils in both the MHz and GHz ranges (Mironov & Savin, 2015).

Distinguishing between mineral and organic-rich soils as well as between frozen and thawed conditions is important due to distinct dielectric behavior in all these cases. Organic material differs from mineral by its complex structure and small bulk density, high porosity and large specific surface area. These properties lead to extreme water holding capacities up to 0.8–0.9 m^3/m^3 compared to around 0.4–0.6 m^3/m^3 in the case of mineral soils (e.g. Kellner & Lundin, 2001; Li et al., 2004), as well as a higher fraction of bound water. The ability to align with an applied electric field (referred to as polarizability) is considerably reduced in the case of water molecules close to solid surfaces (Jones et al., 2002). Consequently, the relative permittivity of bound water is significantly smaller than that of free water, approaching that of ice. This implies that the bulk relative permittivity of organic substrates with large specific surface areas is lower than in the case of mineral soils (apart from very clayey soils), and the same accounts for frozen versus thawed conditions. Given that organic and frozen soil characteristics are specifically abundant in Northern environments, in these regions special attention should be paid to the application of an appropriate soil water–relative permittivity relation in remote sensing retrieval schemes. This issue was extensively studied in the European Space Agency's SMOSHiLat (SMOS High Latitude) project (Bircher et al., 2015; Bircher et al., 2016). The work is now being continued in order to (1) validate the derived "organic" soil water–relative permittivity empirical model in the SMOS Soil Moisture L2 Prototype Processor, as well as (2) study the approach's potential to be integrated in the operational processor to replace the applied dielectric model for mineral soils over areas with distinct organic soil surface layers.

In L-MEB, the model of Dobson et al. (1985) revised by Peplinski et al. (1995), was used in combination with a simplified approach proposed by Matzler (1998) for sandy soils since the beginning of the SMOS mission. The main input model parameters were SM, soil temperature, soil salinity, bulk density, and % of sand and clay. Since April 2012 (i.e. since version 5.5 of the Level 2 algorithm), the Dobson model was replaced by the Mironov model (Mironov et al., 2012), where the input parameters are limited to SM, soil temperature and % clay. The analysis by Mialon et al. (2015) using datasets from a wealth of world-wide validation sites could not conclude which model performed best. However, the Mironov model was selected as (i) it requires fewer input parameters making it less sensitive to inaccuracies in global soil property maps (soil density in particular), (ii) it is a more physical-based modelling approach of mixing dielectric effects (through the GRMDM model), and (iii) it has been validated over a wider range of soil texture (in particular the range was extended to sand fraction larger than 50%). A key consequence of the use of the Mironov model instead of the Dobson one, was that higher dielectric constants were simulated globally, leading to higher retrieved SM values by ~ 0.033 m^3/m^3 on average at the global scale (Mialon et al., 2015).

The better performance of the Mironov model compared to the Dobson model was demonstrated in several recent studies at local scale from experimental data (Wigneron et al., 2011, Montpetit et al., 2015, Srivastava et al., 2016). In particular, better performances were found for very sandy soils (Bircher et al., 2012, 2017) and for organic-rich soils in Northern environment (Bircher et al., 2015). Note that an unrealistic behavior of the imaginary part of the dielectric constant as a function of SM was clearly detected for the Dobson model (Bircher et al., 2017). Improved simulations of TB were obtained too at global scale using the Mironov model rather than the Dobson one at both C- and L-band (de Rosnay et al., 2009, 2013). These different results support the choice of the Mironov model in the soil moisture retrieval algorithms of both SMOS and SMAP; this latter uses the Mironov model in its baseline Level 2 & 3 algorithms. In contrast, the dielectric model by Wang and Schmugge (1980) is used in the SMAP Level 4 algorithm and in LPRM (Van der Schalie et al., 2015, 2016) and it is considered as an option at ECMWF within the CMEM (Community Microwave Emission Model) modelling platform (de Rosnay et al., 2009; Muñoz-Sabater et al., 2011).

4. Vegetation radiometric modelling

In this section a review of the models used to account for the radiative effects of vegetation at L-band is presented. Firstly some background is presented including the models used in the SMOS and SMAP retrieval algorithms, and secondly recent findings in this domain are presented and analyzed.

4.1. Background

To account for vegetation effects, both the SMOS and SMAP mission use a simple Radiative Transfer (RT) model, hereafter referred to as the τ-ω model. In this model, optical depth τ_P and effective scattering albedo ω_P (p = H, V) are used to parameterize extinction and scattering caused by the canopy layer above the soil (Mo et al., 1982). This model is a zero-order solution of the RT equations, where the phase matrix term accounting for multiple scattering effects, is neglected (Tsang et al., 1985; Ulaby et al., 1986). The rationale for the selection of the latter model is discussed in detail by Wigneron et al. (2007).

In the τ-ω model, the thermal emission TB_P from a scene consisting of a vegetation layer above an infinite half space representing the subjacent soil medium can be written as the sum of three terms: (1) the direct upwelling vegetation emission, (2) the downwelling vegetation emission reflected by the soil and attenuated by the canopy layer, and (3) upwelling soil emission attenuated by the canopy:

$$TB_P = (1-\omega_p)\ (1-\gamma_p)\ (1+\gamma_p\Gamma_{gp})\ T_C + (1-\Gamma_{gp})\ \gamma_p T_g \quad (13)$$

where T_G and T_C are the effective soil and vegetation temperatures, Γ_{GP} is the soil reflectivity and γ_P is the vegetation transmissivity, computed from the optical depth τ_p using Beer's law:

$$\gamma_p = \exp(-\tau_p/\cos\theta) \quad (14)$$

If it is assumed further that the effective scattering albedo ω is equal to zero and that T_G is equal to T_C ($T_G = T_C = T_{GC}$, where T_{GC} is the effective ground-canopy temperature), Eq. (13) can be rewritten in a very simple form as:

$$TBP = (1-\gamma_P^2\Gamma GP)\,TGC \quad (15)$$

In the RT model used for the Level 2 and 3 SMAP products, τ_P equals the optical depth at nadir and it is assumed to be polarization independent for now, whereas it is made polarization dependent in the SMAP Level 4 product. In L-MEB, used by the SMOS mission, τ_P is expressed as a function of the optical depth at nadir τ_{NAD} (at $\theta = 0°$) by:

$$\tau_P(\theta) = \tau_{NAD}\left(\sin^2(\theta)\cdot tt_P + \cos^2(\theta)\right)\ (P = H, V) \quad (16)$$

where the tt_V and tt_H parameters allow for the dependence of τ_P on incidence angle θ to be accounted for, which can be different according to polarization, particularly for vegetation with specific anisotropic structures. This formulation was based on the modelling of the vertical stalk layer as a uniaxial crystal (Allen & Ulaby, 1984; Ulaby & Wilson, 1985). A value of $tt_P > 1$ or $tt_P < 1$ will correspond, respectively, to an increasing or decreasing trend of τ_P as a function of θ. The "isotropic" case, where τ_P is assumed to be independent of polarization and incidence angle corresponds to $tt_H = tt_V = 1$. The latter case is currently used in the SMOS algorithm (Table 1).

The use of the polarization dependent tt_P (P = H, V) parameters was developed to account for the effects of vegetation anisotropy on optical depth with respect to incidence angle and polarization, which were found to be very significant for crop types with vertical (stem-dominated) structure, such as cereals and corn (Wigneron et al., 2004; Fig. 5). For instance the optical depth of a well-developed wheat canopy was found to be three times higher at V- than at H-polarization (0.3 vs. 0.1) (Fig. 5; Wigneron et al., 2004) and a good linear relationship between the tt_V parameter and the height of stems was estimated during the growth of a wheat canopy ($R^2 = 0.97$).

The τ-ω model equations have some limitations. First, in theory, the τ - ω equation (Eq. (13)) cannot account for multiple scattering effects. However, Mo et al. (1982) showed, through the delta Eddington approximation, that the equations of the τ-ω model are valid with the assumption that scattering by the vegetation elements is primarily in the forward direction. They showed also that, in this case, the τ_P and ω_P parameters are effective parameters that can be estimated from the fractional scattering along the forward direction. In addition, the τ-ω model inherently assumes small dielectric gradients between the air and the vegetation layer, implying that both reflection and refraction at the air-to-vegetation interface are neglected. While this so-called 'soft-layer' assumption is valid for L-band observations of a vegetation layer, with mostly very low vegetation volume fraction (Wigneron et al., 1993), the 'soft-layer' assumption is not adequate in the presence of a litter or a snow cover. To simulate upwelling TB_P (P = H, V) of a ground covered with such a dense and/or possibly scattering layer, a higher-order solution of the RT equations should be used. The so-called 'two-stream' (2S) RT model (Wiesmann & Mätzler, 1999) originally developed as a part of the Microwave Emission Model for Layered Snowpack (MEMLS), poses an option and the use of the 2S RT model in substitution of the τ-ω model in L-MEB is currently being tested. This substitution would allow using a consistent RT model to simulate the emission from grounds covered with vegetation, litter, or dry snow (Lemmetyinen et al., 2016), leading to a unification of the retrieval scheme applied to a variety of land-cover types.

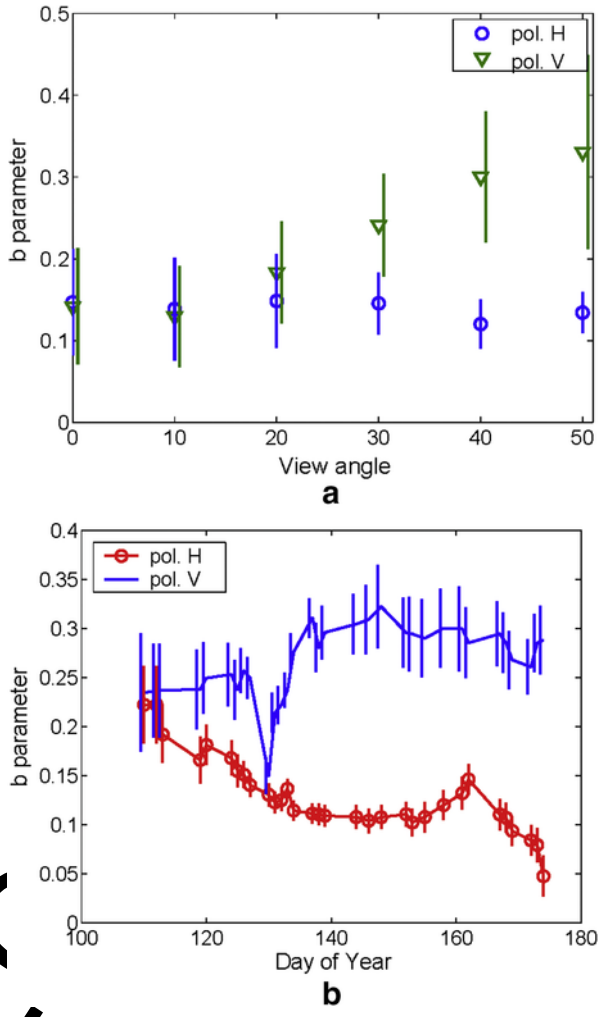

Fig. Dependence of the b parameter on (a) incidence angle and polarization and (b) Day of Year (well-developped wheat canopy, PORTOS-93 experiment; adapted from Wigneron et al., 2004).

4.2. *Effective scattering albedo*

Note that, following Kurum (Kurum, 2013), the term 'effective scattering albedo' for ω_P is used rather than the term 'single scattering albedo' which can be often found in the literature. The difference in meaning of the two is important as follows: the term 'effective

scattering albedo' means the value of ω_P that best represents scattering effects in TB_P (θ) simulated with the τ-ω RT model in comparison with either experimental brightness temperatures, or corresponding numerical simulations. Accordingly, 'effective scattering albedo' ω_P can be computed, through calibration using experimental (Wigneron et al., 2004) or numerical (Ferrazzoli et al., 2002) data, or based on physical considerations (Kurum, 2013). Conversely, the 'single scattering albedo' is defined as the ratio between the scattering coefficient and the extinction coefficient (including both scattering and absorption) and is used in multiple scattering RT models (Wigneron et al., 1993). Values of 'single scattering albedo' (~ 0.20–0.50) are generally larger than values of 'effective scattering albedo' for most vegetation canopies (Ferrazzoli et al., 2002; Kurum et al., 2011).

Recently, Kurum (2013) removed the restrictions that were posed by the original model of Mo et al. (1982) that assumes scattering by the vegetation is primarily in the forward direction (Joseph et al., 1976). He showed that the τ-ω model equations are correct in their analytical form without making assumptions on the scattering pattern, as done by Mo et al. (1982), provided ω_P is considered as the 'effective scattering albedo' as defined above. So, even if values of ω_P are generally calibrated from best-fit approaches, they have a clear physical meaning. Note that over forests, this result was numerically demonstrated by Ferrazzoli et al. (2002), who successfully calibrated 'effective vegetation parameters' (τ_P and ω_P) of the τ-ω RT model using a discrete RT model applied to simulate $TB_P(\theta)$ of forested scenes. The calibration of the effective scattering albedo is analyzed in the two following sections from, respectively, tower-based and space-borne observations

4.2.1. Tower-based calibration of ω

Based on measurements performed with tower based L-band radiometers, the values of the effective scattering albedo ω_P at L-band have generally been found to be low, except for corn (ω_P ~ 0.05–0.10; Wigneron et al., 2004; Wigneron et al., 2007; Yan et al., 2015) and for grass (ω_P ~ 0.10; Saleh et al., 2007) at V polarization. These values are in good agreement with the values of the 'effective scattering albedo' ω_P computed by Kurum (2013) at L-band for a corn (Cf Fig. 6) and a soybean canopy from discrete RT simulations. For instance, Kurum (2013) found that the values of ω_p for corn are slightly depen-

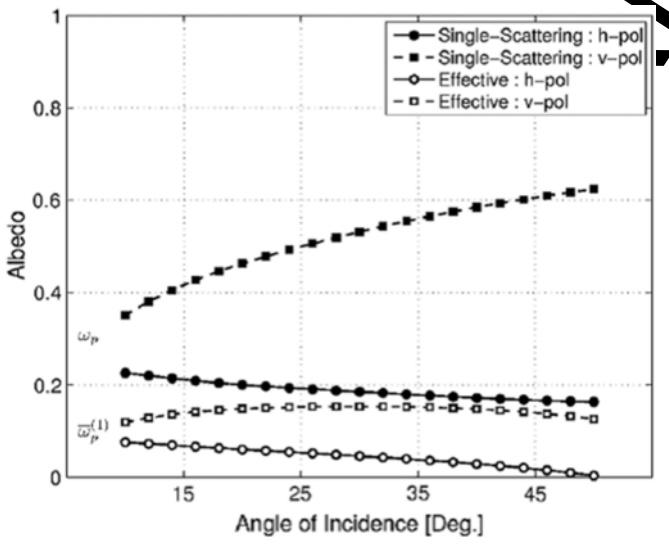

Fig. 6. Single-scattering (solid symbols) and effective single-scattering albedo (open symbols) values (calculated at SM = 0.20 m^3/m^3) as a function of incidence angle for both polarizations (P = H, V), for a well-developed corn canopy (Kurum, 2013).

dent on incidence angle and soil moisture and vary between 0.05 and 0.10 at H polarization and between 0.10 and 0.15 at V polarization. He found lower values of ω_P for a soybean canopy, being a leaf-dominated vegetation ($\omega_P \leq 0.02$ at H polarization and $\omega_P \leq 0.05$ at V polarization).

The dependence of ω_P on polarization P = H, V has often been neglected in the literature (in the following the subscript "P" will generally be left out). However, when these effects are accounted for over low vegetation covers, results generally go in the direction of higher scattering effects (and associated values of ω_P) for V polarization vs. H polarization. For instance, the polarization dependence of ω_P was clearly noted over grassland where $\omega_H \sim 0.00$, and $\omega_V \sim 0.05$–0.15 (Lievens et al., 2015; Saleh et al., 2007); it was found to be more moderate over cropland (Kurum, 2013; Lievens et al., 2015) and forest (Ferrazzoli et al., 2002; Grant et al., 2008; Lievens et al., 2015; Roy et al., 2012). The time variations in ω_P, even though they may be significant over crop fields (Wigneron et al., 2004), are generally neglected too in the literature.

4.2.2. Calibration of ω from space-borne observations

Presently, in the SMOS algorithm, the values of ω_P are tabulated as a function of vegetation class with a default value of zero over low vegetation canopies and 0.06–0.08 over forests. In the SMAP algorithm, values of ω are tabulated for 12 main IGBP vegetation types (Table 3).

The analysis of these calibrated values is not easy, as few studies can be found in the literature at global scale, with very recent results just now available. For instance, the SMAP Level 4 product provides global maps of ω (Chaubell et al., 2014, Fig. 7a) obtained through calibration with SMOS data (currently, using 5 years of SMOS V620 TB data), as described in De Lannoy et al. (2013, 2014). The global average and standard deviation of the ω values (not polarization dependent) for the SMAP L4 product is 0.09 ± 0.07 (Table 3, Fig. 7a). Another recent map of ω has been published by Konings et al. (2016) and is presented in Fig. 7b. The latter study is based on the use of

Table
Values of the 'effective scattering albedo' (ω) as considered in current SMOS (Kerr et al., 2014; Kerr et al., 2012) and SMAP Level 2 & 3 retrieval algorithms (O'Neill et al., 2015) and retrieved in the recent studies of Konings et al. (2016) and for the SMAP Level 4 product (following De Lannoy et al., 2014).

Land cover type	'Effective scattering albedo' (ω)			
	SMOS algorithm (current, default)	SMAP L2 & 3 algorithm	Konings et al. (2016) (from Aquarius data)	SMAP L4 algorithm (from SMOS data)
Evergreen needleleaf forest	0.06–0.08[a]	0.050	0.05	0.12
Evergreen broadleaf forest	0.06–0.08[a]	0.050	0.05	0.08
Deciduous needleleaf forest	0.06–0.08[a]	0.050	0.06	0.12
Deciduous broadleaf forest	0.06–0.08[a]	0.050	0.03	0.10
Mixed forest	0.06–0.08[a]	0.050	0.05	0.12
Closed shrublands	0.00	0.050	0.03	0.14
Open shrublands	0.00	0.050	0.05	0.11
Woody savannas	0.00	0.050	0.04	0.13
Savannas	0.00	0.080	0.02	0.12
Grasslands	0.00	0.050	0.03	0.07
Croplands	0.00	0.050	0.04	0.12
Cropland/natural veg. mosaic	0.00	0.065	0.02	0.15
Barren or sparsely vegetated	0.00	0.000	–	–

[a] ω = 0.08 over boreal forests, ω = 0.06 over the other forest types.

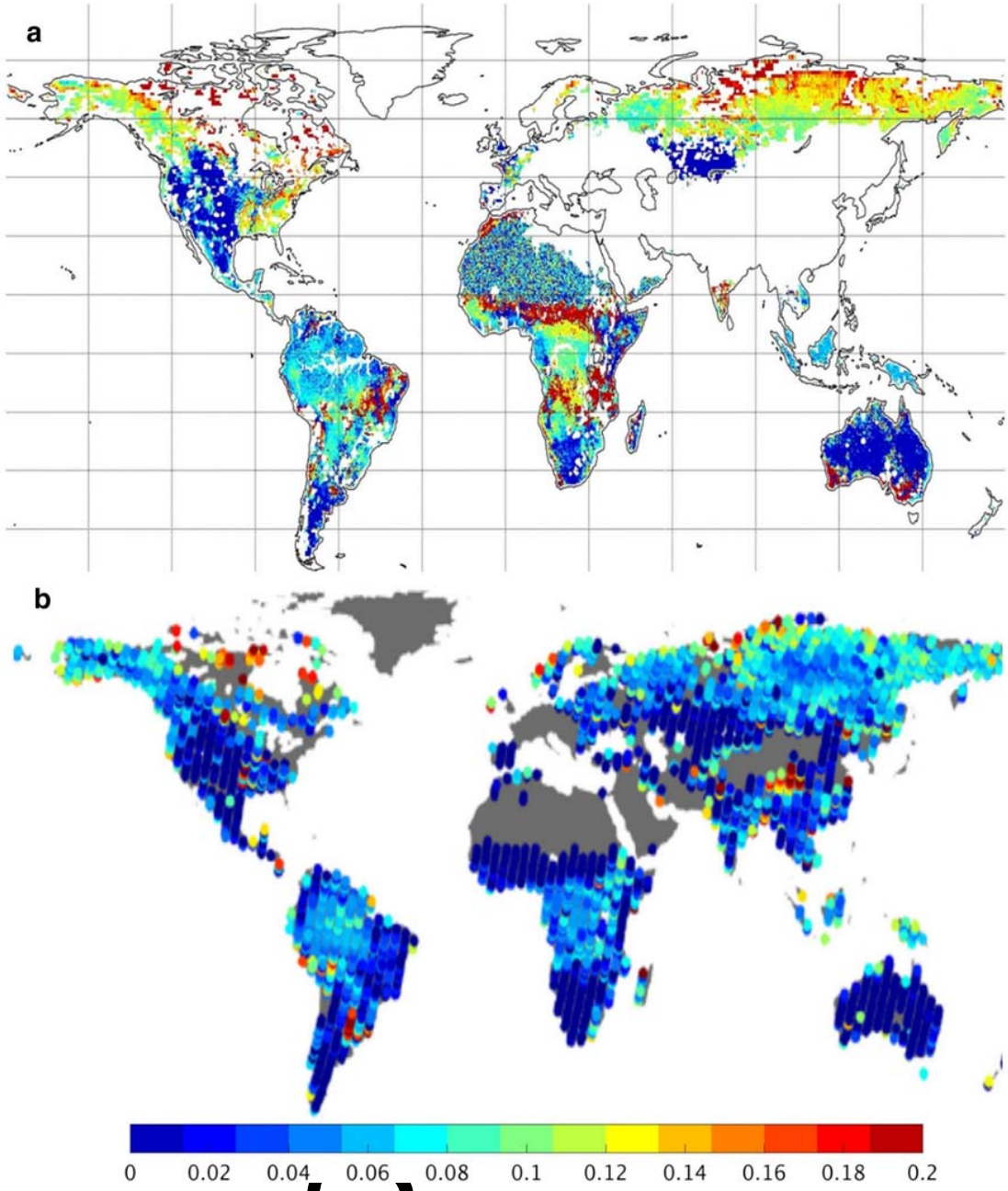

Fig. 7. Global map of effective scattering albedo at L-band retrieved from the (a) SMOS TB data (SMAP L4_SM product; De Lannoy et al., 2014) and (b) Aquarius (Konings et al., 2016) observations.

multi-temporal single look-angle Aquarius observations to retrieve three parameters (SM, τ and ω) without the need of optical ancillary information. The authors found a high variability in the values of ω per land use class: values are in the range 0.02–0.04 over low vegetation (grassland, cropland) and 0.03–0.06 over forests. The estimated values in Fig. 7a and b differ most likely because of different assumptions for the other RT parameters and/or the ancillary information and because of the different temporal and spatial resolutions of the SMAP and Aquarius instruments. These results are summarized in Table 3.

Recently, van der Schalie et al. (2016) optimized the values of ω globally in the LPRM algorithm based on SMOS observations and did not see the benefit of spatially varying values: they found an optimized global value ω = 0.12. Current studies are being made too to update the values of ω in the SMOS algorithm (Fernandez-Moran et al., 2016). In very good agreement with the results obtained by van der Schalie et al. (2016), Fernandez-Moran et al. (2016) found a rather low sensitivity of ω to the IGBP vegetation classes, with a global optimized values ω = 0.10. The values of ω obtained by these studies from space-borne observations at L-band are in the higher end of the range of values (~ 0.00–0.012) obtained from tower-based experiments over both low vegetation and forest canopies. An explanation of this could be that, in the RT modelling, the relatively high values of ω could be an "effective" way to account for the heterogeneity of the soil and vegetation signatures within the large footprint of space-borne observations.

At higher frequencies, values of ω_p varying between 0.05 and 0.10 were found by Pellarin et al. (2006) over a large variety of canopy types (including crops, grasslands and forests) based on SMMR (Scanning Multichannel Microwave Radiometer) observations at C- and X-bands. In addition, Du et al. (2016) have computed values of ω (not polarization dependent) accounting for its seasonal variations from the AMSR-E observations at X-band. They found a quadratic relationship between ω and τ, with average values of ω varying between 0.04 and 0.06 at global scale (Fig. 8). Du et al. (2016) considered that multiple scattering effects lead to increasing vegetation emission, leading in turn to lower values of effective ω. So, for very dense vegetation, due to overwhelming multiple scattering effects, ω tends to be saturated and becomes relatively stable at ~ 0.06. These results are consistent with the values of ω found by Pellarin et al. (2006) (~ 0.06–0.08) and Roy et al. (2012) (~ 0.06) over boreal forests.

4.3. SMOS and SMAP vegetation optical depth

As already mentioned in Section 2, it is considered in the SMAP algorithm that Vegetation Water Content (VWC, $kg \cdot m^{-2}$) is a good proxy to compute the vegetation optical depth. Optical depth at nadir is computed as $\tau_{NAD} = \tau\ (\theta = 0°) = b * VWC$ where the value of the so-called 'b-parameter' is approximately b = 0.12 (± 0.03) $kg^{-1}\ m^2$ for a large variety of vegetation types (Jackson & Schmugge, 1991; Van de Griend & Wigneron, 2004). However, some studies found that the value of b may vary during the vegetation cycle. For instance, Wigneron et al. (2004) found the value of b was lower during the senescence period over crop fields (Cf Fig. 5) and Schwank et al. (2005) demonstrated the dependence of b on the growing state of clover grass.

In the SMOS algorithm, generally a 2 parameter (2-P) inversion process of soil moisture (SM) and optical depth at nadir (τ_{NAD}) is carried out. However, for some specific configurations of the inversion process it is necessary to compute τ_{NAD} (for instance, at the edge of the Field of View where only a narrow range of viewing incidence angles is available for the 2-P inversion process, Kerr et al., 2012; Wigneron et al., 2000). In the SCA algorithm used for SMAP, the optical depth τ_{NAD} is not retrieved, but it is estimated from ancillary information. More specifically,

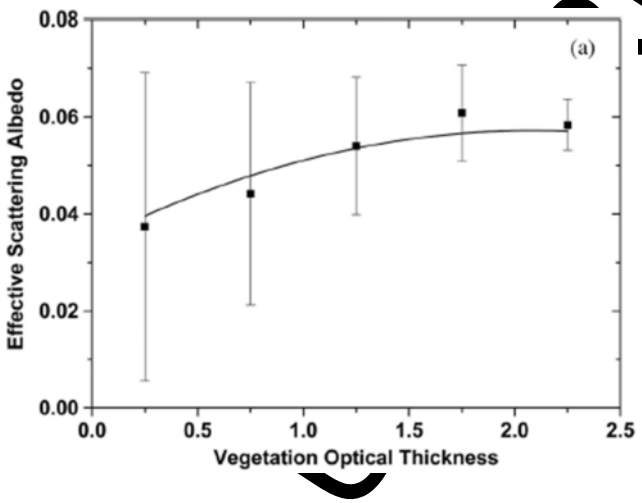

Fig. 8. Averaged effective scattering albedo retrieved from AMSR-E observations at X-band, as a function of the vegetation optical thickness considering five optical thickness subgroup levels. Squares are the median of the range, the line corresponds to a fit of the averaged albedo values, and error bars denote the standard deviation of the albedo values within each corresponding optical thickness subgroup (Du et al., 2016).

(i) In the SMAP SCA algorithm, the vegetation water content VWC is computed from NDVI (Jackson et al., 2004) while the 'b-parameter' is estimated using a look-up table based on the IGBP Land cover classification (O'Neill et al., 2015).

The following equation is used to compute VWC (kg/m²) (O'Neill et al., 2015):

$$VWC = \left(1.9134 \cdot NDVI^2 - 0.3215 \cdot NDVI\right) + Stemfactor \cdot \left(NDVI_{ref} - 0.1\right) / (\ldots - 0.1) \quad (17)$$

where the Stemfactor parameter is the product of the average height of a land cover class and the ratio of stem/wood area to leaf area; $NDVI_{ref}$ is assumed to be equal to the maximum value of NDVI time series, except over croplands and grasslands where the current NDVI can be used for $NDVI_{ref}$. A global 5-year MODIS NDVI climatology at 1 km spatial resolution is used currently to provide NDVI values for VWC estimation in the SMAP operational processor. An assessment will be made by the SMAP team as to whether to use real-year NDVI in lieu of the NDVI climatology in the final bulk reprocessing of SMAP data.

(ii) In the SMOS algorithm a linear relation between τ_{NAD} and LAI is considered according to

$$\tau_{NAD} = b' \cdot LAI + b'' \quad (18)$$

where the parameters b′ and b″ are assumed to depend mainly on the vegetation type. From tower-based L-band observations made over crop fields, Saleh et al. (2006) and Wigneron et al. (2007) found the value $b' \approx 0.06$. Note that considering $b \approx 0.12$ in Eq. (1), the use of $b' = 0.06$ and $b'' = 0.00$ leads to estimate that VWC ≈ 0.5. LAI (currently the value b′ = 0.06 is used as a default parameter in L-MEB for all vegetation types). As mentioned above, this equation is used marginally in the SMOS algorithm for some specific configurations of the inversion process and should be needless in future versions of the SMOS algorithm.

4.4. Low vegetation optical depth

4.4.1. LAI- and NDVI-based estimation of optical depth at nadir (τ_{NAD})

In the SMOS, DCA and LPRM algorithms, vegetation optical depth (τ) is retrieved concurrently with SM. However, the τ parameter is required in the SCA algorithm (as used for SMAP L2&3). So, parameterizing τ as a function of vegetation indices (such as LAI and NDVI) is a key step for this latter algorithm. Following the study by Wigneron et al. (2007), the calibration of the b′ and b″ parameters in Eq. (18) has been mainly made from tower-based experiments. For instance, Schlenz et al. (2012) found that b′ = 0.12 and b″ = 0.08 for winter oilseed rape.

At a larger scale, the values of b′ and b″ used in L-MEB have been analyzed from SMOS observations over crop zones in Central USA by Lawrence et al. (2014) who estimated an average slope of b′ = 0.06 and an average intercept of b″ = 0.14. Grant et al. (2016) have recently analyzed the relationship between the SMOS and AMSR-E vegetation optical depth (respectively τ_{SMOS}, derived from L-MEB inversion and $\tau_{AMSR\text{-}E}$, derived from the LPRM method) and MODIS-based vegetation indices: LAI, NDVI, Enhanced Vegetation Index (EVI), and Normalized Difference Water Index (NDWI). Non-linear relationships were obtained in some cases, which is in

agreement with (Gao et al., 2015; Jones et al., 2011; Liu et al., 2011):

(i) $\tau_{AMSR\text{-}E}$, computed from C-band observations, reveals some saturation effects earlier than τ_{SMOS}, computed from L-band observations, as the value of the vegetation index increases.
(ii) The vegetation indexes computed from optical observations saturate at high levels of LAI.

At global scale, over the year 2010, Grant et al. (2016) found that highest correlations between optical depth and vegetation indexes (LAI, NDVI, EVI, NDWI) for both SMOS and AMSR-E sensors were obtained using the NDVI index (Fig. 9). However, the relationship between τ_{SMOS} and NDVI (R = 0.69) is nonlinear whereas that between τ_{SMOS} and LAI is linear and presents a similar correlation coefficient (R = 0.68), for which reason Grant et al. (2016) consider that LAI may be the preferred choice of vegetation index in the case of SMOS.

4.4.2. *Structural parameters tt_V and tt_H*

Several recent studies have shown that the vegetation structure effects may have an impact on the values of optical depth and found that the dependence of τ_P on incidence angle and polarization could be well parameterized using different values for tt_V and tt_H in Eq. (16). Peischl et al. (2012) showed very distinct values of tt_P (P = H, V) in SM retrievals over wheat canopies (tt_H = 0.2, tt_V = 1.4) in New South Wales, Australia. Similarly, Yan et al. (2015) calibrated a value of tt_V = 3.0 to simulate the emission from corn fields in the Heihe River Basin in Northern China. Over a vineyard, Saleh-Rastkhani et al. (2012) observed large differences between tt_V and tt_H in winter (tt_V ~ 0.80 and tt_H ~ 0.11), whereas the tt_V and tt_H parameters have similar and larger values in summer (tt_V ~ 1.40 and tt_H ~ 1.10). These seasonal differences could be related to changes in the structure of the vine stocks, while the leafy vegetation in summer is more isotropic (tt_V and tt_H values are close to 1.0). Pardé et al. (2004) over corn and Fernandez-Moran et al. (2015) over vineyard showed that temporal changes in the tt_V parameter can be accounted for using a 3-parameter inversion approach where SM, τ_P and tt_V are retrieved independently. All the aforementioned studies were based on tower-based radiometer measurements and simultaneous in-situ observations of vegetation properties. From space-borne instruments, the large footprint of microwave radiometers include a variety of vegetation and soil types, so that vegetation structure effects are not generally accounted for (Owe et al., 2001). Presently default parameters neglecting these effects are used both in the SMOS retrieval algo-

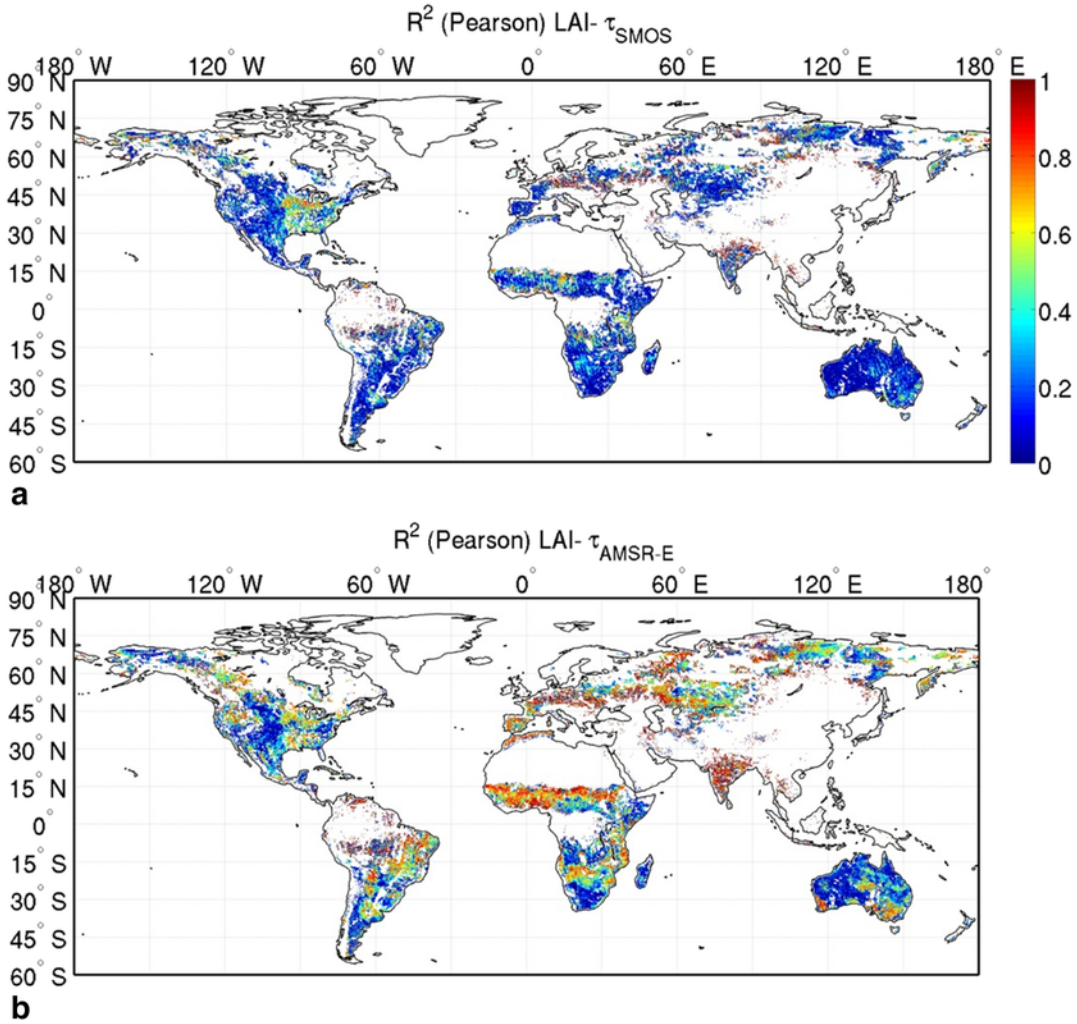

Fig. 9. Pixel-based Pearson coefficient of determination (R^2) for the relationship between LAI and 16-day average values of optical depth in 2010 retrieved from (a) SMOS (ascending orbits) and (b) AMSR-E (ascending orbits) observations. White areas indicate "no data". (details of the computations are given in Grant et al., 2016).

rithm ($tt_V = tt_H = 1$) and the SMAP retrieval algorithm assuming isotropic vegetation with $\tau_V = \tau_H$.

4.5. Forests: specific modelling aspects

Forests show several specific issues, making the modelling of TB more challenging than for scarce vegetation. This topic was theoretically investigated by Ferrazzoli and Guerriero (1996), Karam (1997) and Kurum et al. (2011, 2012). In forests, both single and multiple scattering effects are appreciable, and cannot be neglected at any frequency, including L band. Moreover, absorption and scattering effects are mostly due to branches, which are characterized by a wide distribution of sizes and orientation, and by permittivity properties which are different with respect to herbaceous vegetation. Conversely, polarization effects are low, so that we can assume: $\omega_H = \omega_V = \omega$; $\tau_H = \tau_V = \tau$.

In the SMOS algorithm, a compromise between model accuracy and simplicity was adopted (Kerr et al., 2012; Rahmoune et al., 2013). On the basis of parametric investigations, it was found that the τ-ω RT model (Eq. (13)) can be extended to forests with acceptable accuracy, provided ω and τ are defined as "effective" parameters, in order to include multiple scattering effects (Ferrazzoli et al., 2002; Kurum et al., 2012). In fact, the average single scattering albedo of branches is on the order of 0.40–0.60 (Ferrazzoli et al., 2002; Kurum et al., 2012), values which cannot be directly introduced into the τ-ω model (Eq. (13)), since it would lead to unrealistically low TB_P values, far from measured ones. Ferrazzoli et al. (2002) suggested to fit the vegetation parameters ω and τ used in the τ-ω model to the angular and polarization dependent $TB_P(\theta)$ simulated with a discrete radiative transfer model. This parameter-calibration was adopted in the SMOS algorithm (Rahmoune et al., 2013) to provide first guess values τ^{ini} of optical depth τ and the 'effective scattering albedo' ω, which is assumed to be constant throughout the retrieval. The first guess values τ^{ini} were computed as the sum of a dominant static component, due to branches, and a minor seasonal component, due to leaves and understory. The static component was related to LAI in full development (called LAI_{max}), and the seasonal component was related to actual LAI. Also litter effects were included in τ and related to LAI_{max} (Rahmoune et al., 2013). For the 'effective scattering albedo' at L band, values in the range of $0.08 \le \omega \le 0.10$ were generally found using model simulations and experimental data (Grant et al., 2008; Santi et al., 2009), although higher values were obtained in some experiments (Kurum et al., 2012).

These first estimates of the forest RT parameters (ω and τ) were compared against SMOS retrieval results obtained using the standard L2 algorithm and an off-line algorithm operating in a 3-parameter mode to retrieve the 'effective scattering albedo' ω in addition to SM and τ (Rahmoune et al., 2013). The retrieved optical depth was found to be slightly lower than initial estimates of τ^{ini} based on LAI. At continental scale, the retrieved τ value was found to be well correlated with forest height data obtained by space-borne LiDAR (Light detection and ranging) measurements (Rahmoune et al., 2014; Vittucci et al., 2016). At regional scale, even better correlations were found with biomass data estimated by airborne LiDAR measurements (Vittucci et al., 2016). As an example, Fig. 10 reports a scatterplot of retrieved τ as a function of measured biomass for forest areas in Peru and Columbia.

Retrieved values of the 'effective scattering albedo' turned out to be slightly lower than values initially estimated in Ferrazzoli et al. (2002). A value of ω = 0.06 provided best results, particularly in tropical forests (Rahmoune et al., 2013). A parallel investigation based on radiometric Aquarius signatures (Konings et al., 2016) indicated the average 'effective scattering albedo' of dense forests to be ω = 0.05,

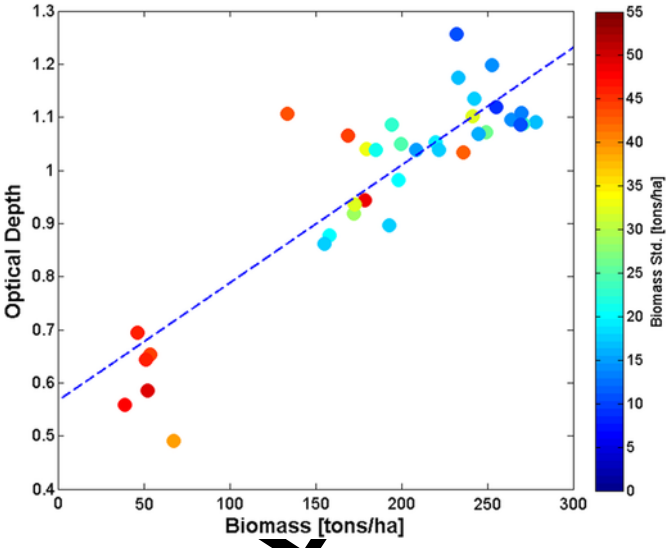

Fig. 10. Scatterplot of SMOS retrieved τ and forest biomass measured in forest pixels of Peru and Columbia. Color codes indicate the standard deviation of measured biomass within SMOS pixel (R^2 = 0.74) (Vittucci et al., 2016).

while the obtained map of optical depth τ_P showed spatial patterns similar to the ones found by Rahmoune et al. (2013) and Vittucci et al. (2016). As for SMAP higher level products, after calibration with V620 SMOS TB data a global average ω = 0.10 was found over dense forests and used in the SMAP L4_SM product (Entekhabi et al., 2010). For the L2 and L3 SMAP soil moisture products, ω = 0.05 is currently used as a default for forest categories of land cover while the SMAP team focuses on retrieval performance for nonforest land covers. Efforts will be made in the near future to understand and improve SMAP retrievals over forests with a goal of making the retrievals more consistent with SMOS retrievals (Jackson et al., 2016).

Investigations were also conducted at higher frequencies. As expected, retrievals of τ were found to be generally higher than at L-band. It was also found that the leaf contribution increases with frequency more than the trunk and branch contributions (Guglielmetti et al., 2007; Santi et al., 2009). The emissivity of developed forests increases with frequency (Guglielmetti et al., 2008; Macelloni et al., 2001; Santi et al., 2009), and this property can be represented by a decrease of the 'effective scattering albedo'. A theoretical explanation of this result was given by Della Vecchia et al. (2010). When frequency increases, scattering effects increase too, but in forests they tend to be in the forward direction. In consequence, this leads to a decrease of scattered radiance into the upper half space. The latter, in turn, decreases the overall canopy reflectivity, and hence explains the higher forest emission at higher observation frequencies.

4.6. Interception, litter

The vegetation optical depth modelling approach presented in the previous sections need to be extended, in order to account for some specific effects linked to water interception by the canopy and litter. Litter is present in most vegetated ecosystems where the soil is not worked mechanically. The effect of intercepted water, both by the standing vegetation and litter, may have an impact on the upwelling microwave radiation TB_P.

Several experimental results found in the literature cannot be explained without considering interception and/or litter effects. For instance, high values of the 'b-parameter' were computed over grassland covers (b ~ 0.4, Jackson & Schmugge, 1991; Saleh et al., 2006; Schwank et al., 2005; Wigneron et al., 2004). De Rosnay et al. (2006)

found increasing values of L-band brightness temperature TB_P over a fallow field during rainfall events, while at the same time, decreasing values of TB_P were measured over an adjacent bare soil plot. Over the same fallow site, Saleh et al. (2006) found that values of τ_{NAD} may be increased by a factor of 2 to 3 during rainfall events. Conversely to the above results, Hornbuckle et al. (2006) found that water at the plant surfaces of a maize canopy (due to irrigation, rainfall or dew) has the net effect of decreasing TB_P at 1.4 GHz. However, these effects were found to be relatively moderate (TB_P varying by a few Kelvin).

These litter and interception effects were also evaluated in forests, where the litter layer can be very thick for coniferous vegetation types (Grant et al., 2007; Grant et al., 2009; Guglielmetti et al., 2008; Schwank et al., 2008). From passive L-band observations performed above a deciduous forest stand in Jülich (Germany), Guglielmetti et al. (2008) and Schwank et al. (2008) demonstrated that moist litter is an important radiation source to be taken into account for quantitative SM retrievals based on passive L-band data. In the coniferous forest of Les Landes in Southwestern France, Grant et al. (2009) found that the presence of the litter layer over a soil surface can lead to a significant increase in the value of the surface emissivity (~ 60 K in TB) in comparison to the emission of the underlying mineral layer, but did not modify significantly the sensitivity of the TB_P observations to SM. These experimental results are in good agreement with results obtained by Demontoux et al. (2008) from both coherent and incoherent modelling (Fig. 11) and by Bircher et al. (2015) in the framework of the SMOSHiLat study. Both Grant et al. (2008) and Saleh et al. (2006) found that litter effects could be accounted for by considering the H_R parameter (a dependence of the roughness parameter H_R as a function of SM was used by Saleh et al. (2006)). In that case, the H_R parameter becomes an effective parameter accounting for surface effects, in the broadest sense of the term, and depending on SM which is closely related to the moisture content of litter (Grant et al., 2007).

As for interception effects by the standing vegetation canopy, these are generally accounted for by the optical depth, which account for the effects of the water content present within and at the surface of the vegetation elements (Saleh et al., 2006; Wigneron et al., 1996). As it is very complex to account for these effects in TB simulations, Saleh et al. (2006) have proposed to use the polarization ratio (MPDI = $(TB_V - TB_H) / (TB_V + TB_H)$) to filter out periods of strong interception effects. The default value used in L-MEB over a low vegetation canopy corresponds to a threshold value of MPDI = 0.026 (values of MPDI below that threshold value are filtered out). Another alternative is to use ancillary land surface model information to flag or filter out times and locations with high interception or precipitation values. Currently, the flagging of the periods of high interception effects is implemented in the SMOS algorithm, and a flagging for heavy precipitation is included in the SMAP algorithm.

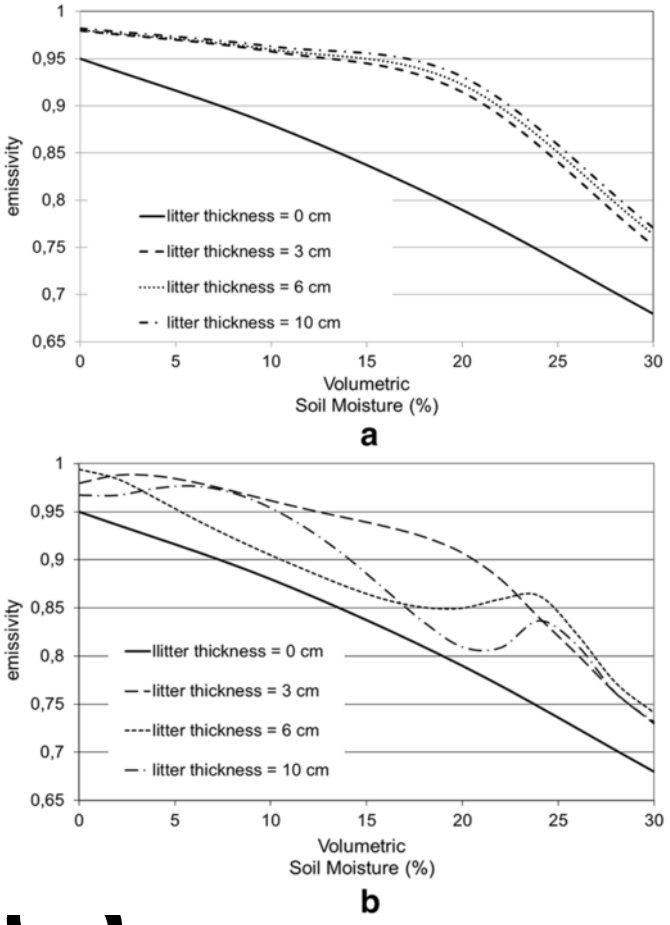

Fig. 1. Emissivity of a soil-litter system as a function of soil moisture for several values of the litter thickness (0, 3, 6 and 10 cm). Computations were made using an incoherent (a) and a coherent (b) model (Demontoux et al., 2008).

5. Combining vegetation and roughness effects

Schmugge et al. (1992) and Jackson et al. (2002) showed that by making some assumptions it is possible to combine the vegetation optical depth (τ_{NAD}) and the soil roughness parameter (H_R) in a single parameter. This very simple formulation can be developed considering that the "effective scattering albedo" $\omega = 0$, and that $Q_R = 0$ and $N_{RV} = N_{RH} = -1$. In that case, the corrections applied in Eqs. (5) and (13) to the soil Fresnel reflectivity ($\Gamma_{GP}^*(\theta)$), due to both the vegetation and roughness effects can be combined and the brightness temperature of the vegetation covered surface can be written as (Parrens et al., 2017):

$$TB_P(\theta) = \left(1 - \exp\left(-\frac{2\,\tau_{NAD} + H_R}{\cos(\theta)}\right)\cdot\Gamma_{GP}^*(\theta)\right)\cdot T_{GC} \quad (19)$$

i.e.

$$TB_P(\theta) = \left(1 - \exp\left(-\frac{2T_R}{\cos(\theta)}\right)\cdot\Gamma_{GP}^*(\theta)\right)\cdot T_{GC} \quad (20)$$

where the combined parameter T_R is defined as $\tau_{NAD} + H_R / 2$.

Note that $H_R = 0$ or $N_{RV} = N_{RH} = -1$ leads to the same results in terms of SM retrievals (mathematically, the equations for $H_R = 0$ or $N_{RV} = N_{RH} = -1$ have the same form, substituting T_R by τ_{NAD} in Eq. (13)).

Recent studies have shown that combining vegetation and roughness effects (using $Q_R = 0$ and $N_{RV} = N_{RH} = -1$) led to best results in SM retrievals over the USA (Parrens et al., 2017) and over a vineyard field (Fernandez-Moran et al., 2015). More studies of this approach are needed. However, if these promising results can be confirmed

there will be clear advantages by using this method. For instance, with the 2-P inversion approach using multi-angular SMOS observations, it would no longer be necessary to calibrate the roughness parameter H_R, as it is included in the combined parameter T_R, retrieved simultaneously with SM. The combined method was used by Wang et al. (2015) and Parrens et al. (2016) to produce global maps of the roughness parameter H_R at, respectively, C-band from AMSR-E observations and L-band from SMOS observations.

One disadvantage of the "combined" approach could be that the retrieved parameter T_R, as it is more sensitive to roughness effects, could be less interesting for monitoring vegetation as done in ecological studies based on the AMSRE vegetation optical depth parameter (Liu et al., 2013, 2015; Tian et al., 2016). However, first analyses investigating this question have not confirmed this hypothesis. For instance, over a vineyard field, the retrieved values of optical depth (τ_{NAD}) are as sensitive to roughness effects as T_R and present a lower temporal dynamic than T_R during the vegetation cycle (Fernandez-Moran et al., 2015). Parrens et al. (2017) found slightly improved correlation between T_R and MODIS NDVI than between τ_{NAD} and MODIS NDVI over numerous sites in the USA. Our interpretation is that roughness (H_R) and vegetation (τ_{NAD}) model parameters cannot be easily distinguished from multi-angular observations over a short period of time: they have a similar impact on the TB signatures (exponential form as given in Eqs. (5) and (14), Cf Parrens et al., 2017). So, to monitor vegetation, these results may indicate that it is preferable to have a good method to retrieve a combined "vegetation-roughness" parameter, than a less performant method considering separately vegetation and roughness effects.

Another approach was recently developed using measurements made during the SMAPVEX12 experiment in Canada, over a variety of crop fields at a constant incidence angle of ~ 40°. Martens et al. (2015) proposed to model H_{RP} as a function of brightness temperature and LAI as:

$$H_{RP} = \left(c_{1P} + c_{2P}\, TB_P + c_{4P}\, LAI\right)^{C3P} \quad (21)$$

where the coefficients c_{1P}, c_{2P}, c_{3P} and c_{4P} where fitted using the experimental data.

The results of this study confirmed those based on the T_R parameter, and showed (i) the need for a dynamic roughness parameter (as opposed to the use of a constant roughness parameter over time) and (ii) the difficulty of decoupling roughness and vegetation effects as H_R also partially accounts for the latter.

6. Soil and vegetation radiometric modelling for operational data assimilation

The assimilation of passive microwave observations into land surface models has the potential to add value to the coarse-scale and intermittent swaths of microwave space-borne observations. The RT model is at the heart of all TB assimilation systems as the observation operator. This forward model is used to relate SM, soil temperature, and vegetation characteristics from a land surface model with TB predictions. Differences between the TB predictions and corresponding observations from either SMOS or SMAP (for example) are used to update SM and soil temperature (and possibly vegetation parameters). These updates are propagated in space and time, and throughout the entire land surface system to obtain enhanced and consistent land surface state and flux estimates, with an increased spatial and temporal coverage compared to that provided by satellite data alone. In addition, data assimilation can increase the spatial resolution of the coarse-scale satellite data through dynamic downscaling to finer resolutions. The objective of cycling SMOS or SMAP data assimilation in the numerical weather prediction context is to initialize the forecast model soil moisture conditions to capture as best as possible the soil moisture dynamics at each grid point of the model.

Both SMOS and SMAP microwave data have been used in (near-) operational land data assimilation systems. These large-scale systems leverage off of early conceptual one-dimensional TB assimilation studies (Entekhabi et al., 1994; Galantowicz et al., 1999) and some larger-scale studies by e.g. Walker and Houser (2001), Reichle et al. (2001), Crow and Wood (2003), Balsamo et al. (2006). The SMOS near-real-time brightness temperature product is used at ECMWF and at Environment Canada for Numerical Weather Prediction applications (Carrera et al., 2015; de Rosnay et al., 2013; Muñoz-Sabater et al., 2012, Muñoz-Sabater, 2015). To this end the Community Microwave Emission Modelling Platform (CMEM) was developed by ECMWF as a low frequency passive microwave forward operator for the Numerical Weather Prediction (NWP) community (de Rosnay et al., 2009). It includes a range of state-of-the-art microwave parameterizations for the soil dielectric constant, effective temperature, vegetation opacity and soil roughness. At ECMWF, CMEM is coupled to the Integrated Forecasting System (IFS) for the purpose of SMOS data assimilation. In Muñoz-Sabater (2015), SMOS TB were assimilated for the first time in the full land-atmospheric coupled IFS. The study was conducted at global scale. Despite the simple approach undertaken in this case study, the feasibility and potential benefits of SMOS brightness temperatures data assimilation in a NWP model was proved. De Rosnay et al. (2013) compared the performances of different dielectric-, opacity- and soil roughness models against the SMOS brightness temperature observations. The study was conducted at global scale and for four years from 2010 to 2013 using SMOS reprocessed data available at that time (V505) and the reanalysis-based CMEM forward simulations to ensure consistent processing of both observed and forward TB. They found that the Mironov and the Wang and Schmugge dielectric mixing models perform similarly and give better results than the Dobson model. This is consistent with results obtained at smaller scales and presented in Section 3.4. The soil roughness model proposed by Wigneron et al. (2001) that accounts for the dependence of the C_T parameter with soil moisture, gives the best performances in terms of simulated TB temporal dynamics. It is used together with the Wang and Schmugge dielectric mixing model and the Wigneron et al. (2007) opacity model in the ECMWF IFS.

Data assimilation methods rely on the assumption that observations and model first guesses are unbiased, so a bias correction is applied before the observations enter the data assimilation. Therefore, the most useful metrics to assess the first-guess departure are the correlation coefficients and unbiased root-mean-square-error (ubRMSE) of time series at each grid point. Fig. 12 shows global maps of ubRMSE between SMOS observations and ECMWF CMEM TB for both polarizations in the SMOS antenna frame, at a 50° incidence angle, for 2010, 2011, 2012 and 2013. A quality control was conducted so that model grid points covered by snow, or with frozen soil, orography, or water bodies covering > 4% of the grid box area are rejected. The SMOS observations flag is also used to reject observations affected by Radio Frequency Interference (RFI). The figure shows annual ubRMSE values ranging from 4 K to 8 K in most areas, indicating a good agreement between the SMOS observations and the ECMWF forward brightness temperatures. Some regions in the Middle East and South-East Asia show larger values of ubRMSE, mostly associated to residual RFI sources. The figure also shows that the extent of RFI affected areas decreases from 2010 to 2013, indicating an improvement in the SMOS data quality between 2010 and 2013

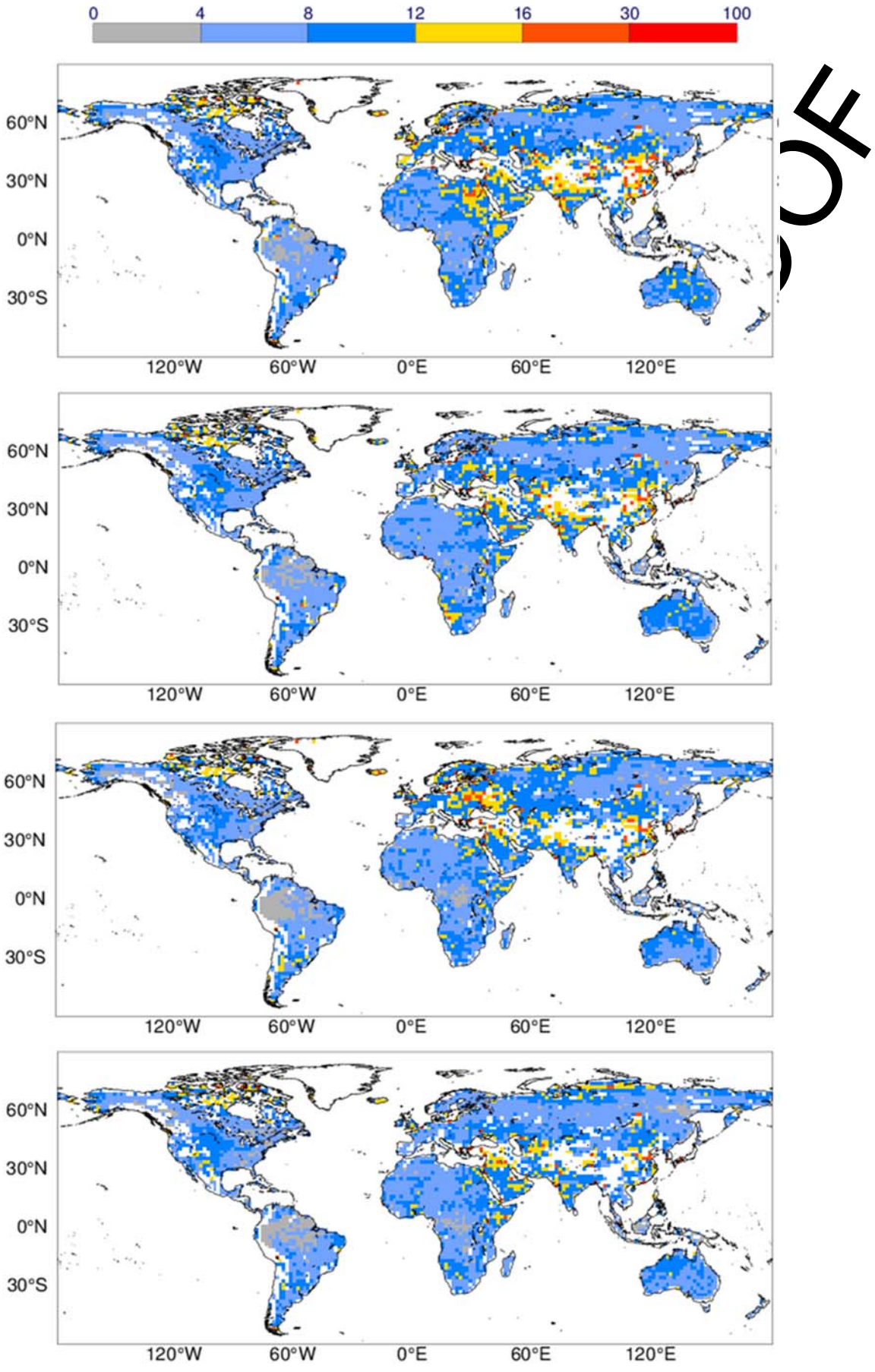
0
4
8
12
16
30
100
60°N
30°N
0°N
30°S
120°W
60°W
0°E
60°E
120°E

which is very relevant for data assimilation activities (global multi-angular statistics are provided in Mecklenburg et al. (2016)).

The SMAP mission includes an operational Level 4 Surface and Root-Zone Soil Moisture product (L4_SM), which is produced by the ensemble-based NASA Goddard Earth Observing System version 5 (GEOS-5) land data assimilation system (Reichle et al., 2015). The L4_SM product assimilates coarse-scale (~ 40 km) SMAP L1C TB data and produces global SM data every 3 h, at 9 km resolution and with a 2–3 day latency. The modelling part of the assimilation system consists of a Catchment land surface model and the τ-ω model. For each grid cell on Earth, τ-ω model parameters (H_{RP}, ω, b_H, b_V) were carefully calibrated using a historical time series of multi-angular SMOS $TB_P(\theta)$ observations, along with estimates of modelling and observation uncertainty to limit over-fitting or parameter compensation for other modelling errors (De Lannoy et al., 2013; De Lannoy et al., 2014). The operational SMAP L4_SM system, calibrated with historical SMOS $TB_P(\theta)$ observations, currently yields SM estimates with ubRMSE well below the imposed 0.04 m^3/m^3 requirement, when compared to in-situ measurements. The study of De Lannoy and Reichle (2015) has confirmed that assimilation of longer time series of multi-angular SMOS $TB_P(\theta)$ in this system improves both the surface and root-zone soil moisture in comparison with model simulations only.

The above examples suggest that the assimilation of brightness temperatures would be the preferred method to update soil moisture estimates. The alternative would be to assimilate soil moisture retrievals, which is generally less complicated to implement. Yet, a key disadvantage of a system that assimilates SM retrievals is that the SM retrievals may be produced with inconsistent ancillary data, such as for example soil temperature simulated by another model than that used in the assimilation system. While in theory brightness temperature assimilation should outperform retrieval assimilation, there is no convincing evidence for it yet for large scale applications (De Lannoy and Reichle, 2016).

7. Summary and discussion

As presented above, significant progress has been made over the last decade in the modelling of passive microwave emission over land surfaces, especially at L-band. This can be explained by the intense scientific activity and the numerous tower-based and airborne experiments, which have been conducted in preparation for the SMOS and SMAP missions, and the fact that time series of TB observations at L-band are now available from space.

The SMOS (end of 2009), Aquarius (mid 2011) and SMAP (beginning of 2015) launches have allowed actual L-band emission of coarse resolution footprints to be analyzed over land surfaces and to develop improved SM retrieval approaches. Previous studies were based on synthetic data sets, based on TB simulations or airborne observations in an attempt to reproduce what could be "seen" by L-band radiometers from space (Pellarin et al., 2003; Wigneron et al., 2000; Wu et al., 2015). The above sections have presented a review of the most significant results obtained in this field, while the following summarizes modelling results and presents a discussion on their possible application to the SMOS and SMAP soil moisture retrieval approaches.

It should be noted that the different studies reviewed here reveal the difficulty of determining any general rules that could be easily applied to estimate vegetation and soil model parameters depending on the vegetation types and soil features alone. Some possible reasons for this difficulty are given in the following:

1) Many significant results were obtained from tower-based experiments at field scale. Even though these studies are interesting in terms of RT modelling and to improve our knowledge of some physical processes, their application to SM retrievals from space-borne observations remains difficult, if not impossible in many cases. In general, the results obtained at a relatively local scale cannot well account for the specific conditions of the space-borne observations, in terms of mixing of soil and vegetation features (land use, local climatic conditions, soil texture, litter, interception, etc.), topographic specific events or conditions (urban and open water areas, snow, frozen conditions).

These considerations might explain the apparent disagreement found between values of the soil and roughness parameters obtained at different scales from tower-based, airborne or space-borne sensors. For instance, optimized values of ω in SM retrievals were consistently obtained in the range of 0.08–0.12 in several recent studies (De Lannoy et al., 2013; 2014; van der Schalie, 2006, Fernandez-Moran et al., 2016). These effective values are in the higher end of the range (~ 0.00–0.12) which has been estimated from tower-based experiments. This result might be related to the heterogeneity of the land use conditions at the scale of very large L-band footprints. Similarly, it is not easy to make a clear link between values of the H_R roughness parameter that have been derived from field experiments (Wigneron et al., 2011, Lawrence et al., 2011) or mapped from space-borne observations (Parrens et al., 2016).

2) Moreover, and this is a topic that would require more attention in future analyses, there is often a disagreement between the values of model parameters (i) calibrated based on TB modelling and (ii) optimized in SM retrievals. This point can be related to model inaccuracies/simplifications which can be partially compensated for by the fact that model parameters are considered as effective. This point can be explained too by the fact that different assumptions are generally made in studies based on TB modelling or in SM retrievals. For instance, optical depth can be retrieved simultaneously to SM, from L-MEB inversion or LPRM, while its simulation in TB forward modelling requires the use of approximate equations (such as Eqs. (17) or (18)).
3) In relation to the above comment, to compare results obtained from different studies (and data sets), methods should be based on similar approaches and hypotheses. In particular, it is not easy to consider separately soil and vegetation effects (in particular soil roughness and optical depth). So, hypotheses made in terms of soil (vegetation) will impact results obtained in terms calibration of vegetation (soil) parameters. For instance, the retrieved value of the roughness parameter H_R may vary, depending on the assumptions made in the calibration of other soil (such as Q_R and N_{RP}) or vegetation parameters (such as ω) (Lawrence et al., 2013). Similarly, higher values of H_R (i.e. stronger roughness effects) may produce lower values of vegetation optical depth

Fig. 12. ECMWF SMOS Brightness temperature monitoring maps at 50° incidence angle, expressed in ubRMSE between SMOS observations and ECMWF CMEM forward simulations, for 2010 (top), 2011 (second panel), 2012 (third panel) and 2013 (bottom panel). The ECMWF CMEM forward computation of brightness temperature accounts for the vegetation effects using the τ-ω model (Wigneron et al., 2007), the soil roughness model follows the Wigneron et al. (2001) parameterization and the Wang and Schmugge (1980) mixing dielectric model is used.

(Fernandez-Moran et al., 2015). The fact that many studies are based on different underlying hypotheses (and calibrated soil/vegetation values) makes it difficult to get convergent results.

4) Finally, with some exceptions (De Lannoy et al., 2014), none of these studies provide statistically meaningful estimates of the uncertainty associated with the estimated parameter values, which prohibits solid general conclusions. Nevertheless, some general "trends", which correspond to a convergence in the results of several studies, can be noted. This convergence is all the more interesting when it can be obtained from different scientific teams, different data sets and different methods. They are summarized and discussed in the two following sections in terms of soil and vegetation.

7.1. Soil

At the field scale, the link between the roughness parameter H_R (the key parameter in the HQN roughness model widely used in microwave remote sensing applications) and the classical geophysical parameters characterizing surface roughness (the standard deviation of heights, S_D, and the auto-correlation length, L_C) is now relatively well known from formulations established at L-band from both empirical and physically-based studies (Lawrence et al., 2013; Wigneron et al., 2010). In addition, the Z_S parameter ($Z_S \equiv S_D^2 / L_C$) was found to be the most pertinent geophysical parameter to parameterize roughness effects in two independent studies in the passive and active domains (Lawrence et al., 2013; Zribi & Dechambre, 2003). The modelling equation $H_R(S_D)$ (Eq. (7)) developed at L-band was found to be valid over a large frequency range (Montpetit et al., 2015), confirming the rather low sensitivity of H_R to frequency (Pellarin et al., 2006; Wang et al., 1983). The values obtained from this formulation are generally in good agreement with the values generally retrieved over low vegetation canopy (Cano et al., 2010; Gao et al., 2013; Saleh et al., 2006; Schlenz et al., 2012).

At the large scale, recent retrieval efforts have used historical time series of SMOS observations to estimate global maps of H_R (De Lannoy et al., 2013; Parrens et al., 2016). Such H_R estimates, along with other RT parameter estimates, are available, for example, as part of the current SMAP L4_SM product (Entekhabi et al., 2014) and will be used in future SMAP Level 2 &3 products. Their use in the future SMOS Level 2 &3 products is currently being investigated (Fernandez-Moran et al., 2016). From these results, it seems there is a convergence of results towards a rather small range of variation in the values on H_R at L-band (~ 0.1–0.5) with lower values obtained for sparsely-vegetated areas (H_R ~ 0.1–0.2) and higher values for forested areas (H_R ~ 0.3–0.45).

A new modelling approach was developed to compute the dielectric constant of the soil, which distinguishes between different states of water in the soil such as free- and bound-water. The same methodology was employed to account for thawed-frozen transitions and organic rich soil conditions (Mironov & Savin, 2015; Mironov & Lukin, 2011; Mironov et al., 2013b). Based on the inter-comparison of dielectric models (Wigneron et al., 2011; Montpetit et al., 2015; Mialon et al., 2015; Srivastava et al., 2013; Bircher et al., 2012, 2015), the dielectric mixing model of Mironov has been implemented in the SMOS (since 2012) and SMAP operational algorithms (Kerr et al., 2012; Jackson et al., 2016; Chan et al., 2016). Note that this is the only key change (April 2012) which was implemented to the L-MEB soil modelling since the SMOS launch. Note also that, to date, very few studies have demonstrated the need to account for the dependence of H_R on polarization (through the N_{RP} parameters) in SM retrievals at the scale of space-borne observations. In addition, we found there is no convergence in studies analyzing the dependence of H_R on SM in SM retrievals from space-borne observations: this is still a key topic of research.

Recent studies have investigated the best strategy to (i) account for soil roughness effects and (ii) to decouple the vegetation and soil effects in SM retrieval studies. Presently, the SMOS and SMAP retrieval algorithms rely on look-up tables providing constant values of H_R for the main land cover types. Recent studies showed the need to consider temporally dynamic values of the roughness parameters H_R and proposed to compute H_R as a function of the vegetation features (LAI or τ_{NAD}), soil moisture and brightness temperature (Martens et al., 2015; Van der Schalie et al., 2016). Other approaches showed the interest of combining the vegetation and roughness effects in the T_R parameter (defined as $T_R \equiv H_R + \tau_{NAD} / 2$), which can be retrieved simultaneously with SM from SMOS multi-angular observations (this case correspond to the use of the roughness parameter $N_{RP} = -1$, at both polarizations). To date, all these options have to be investigated in more depth from space-borne observations before any clear conclusions could be drawn. Note that the current option which is investigated for the SMOS multi-angular observations and which led to promising results is the use of $N_{RV} = N_{RH} = -1$ (Parrens et al., 2016, 2017; Fernandez-Moran et al., 2015, 2016). For that specific configuration, vegetation (τ) and soil roughness (H_R) effects have a similar impact on the TB signatures (same exponential form of attenuation in the RT equations).

7.2. Vegetation

Convergence in the results of several studies considering vegetation are summarized and presented for different items in the following:

7.2.1. Effective scattering albedo (ω)

By computing a first order solution of the radiative transfer equations, Kurum (2013) demonstrated that the τ-ω radiative transfer model is valid in its analytical form to account for multiple scattering effects, provided that ω is considered as an effective parameter. The values obtained theoretically by Kurum (2013) are in good agreement with effective values of ω retrieved over crop fields and grasslands (Lievens et al., 2015; Saleh et al., 2007; Wigneron et al., 2004; Wigneron et al., 2007; Yan et al., 2015) and forests (Grant et al., 2008; Rahmoune et al., 2013). In addition, recent studies found a differentiation between the values of ω at H- and V-polarization, especially over low vegetation covers (Kurum, 2013; Lievens et al., 2015; Saleh et al., 2007).

At large scales and similarly to what was done for the H_R parameter, global maps of the ω parameter (not polarization dependent) have been computed at L-band based on SMOS data (De Lannoy et al., 2013; Entekhabi et al., 2014) and Aquarius data (Konings et al., 2016). At higher frequencies, results obtained by Pellarin et al. (2006), Roy et al. (2012) and Du et al. (2016) from AMSR-E observations seem to indicate a rather low frequency dependence of ω.

The use of these maps in the future SMAP and SMOS Level 2 & 3 products is currently being investigated. Recent studies showed that better characterizing the 'effective scattering albedo' is key in SM retrieval studies from space-borne observations (Davenport et al., 2005, Van der Schalie et al., 2016, Fernandez-Moran et al., 2016). This can be done by parameterizing time constant values of ω as a function of the land cover type (De Lannoy et al., 2014; Fernandez-Moran et al., 2016), or by considering temporally dynamic values of ω using simple relationships (Du et al., 2016) or using 3-Parameter inversion (Konings et al., 2016). Considering that SMOS and SMAP observato-

ries collect microwave data all over the globe, one could expect that a large fraction of the data over land is acquired over vegetation covers whose features can vary both in time and space. In particular, agricultural crops change substantially from planting to harvest. Further studies are therefore needed to establish consistent, physically based global ω estimates over temporally changing vegetated areas (i.e., agricultural crops) for use in the retrievals. Recent studies have optimized ω for SM retrievals from SMOS data (van der Schalie et al., 2016; Fernandez-Moran et al., 2016). They both found high values of ω in the 0.08–0.12 range and a low sensitivity of ω on land use classification in agreement with results of De Lannoy et al. (2014). These convergent results which did not account for time changes in ω should be confirmed in future analyses.

7.2.2. Optical depth

The main difference in the different SM retrieval schemes which have been developed at L-band generally relies on the approach used to account for vegetation effects through optical depth (τ). In the SM retrieval algorithms based on L-MEB, DCA or LPRM, optical depth is retrieved simultaneously with SM, while in the SMAP SCA, optical depth is estimated from the vegetation index NDVI. The interest of retrieving simultaneously SM and τ is three-fold as noted in the initial SMOS concept study (Wigneron et al., 2000):

(i) there is no need for ancillary data on the VWC and b parameters,
(ii) the retrieved parameter τ may turn out to be a very useful product by itself for monitoring the vegetation dynamics, and
(iii) there is a reduced risk to compensate for τ errors in the SM retrievals.

So it is natural to investigate the link between τ_{NAD} and vegetation indices (such as NDVI or LAI) from the SMOS observations for potential application to the SMAP algorithms (for instance to improve the relationships linking τ and NDVI which is used in SCA) and also to evaluate the potential interest of τ in vegetation monitoring. This interest was already noted in many studies based on observations at higher frequencies from AMSR-E (Liu et al., 2013, 2015, Tian et al., 2016, Konings and Gentine, 2016b).

Within the SMOS scientific team, the focus was initially put on SM retrievals, and there is certainly a large margin of improvement with regard to the τ product derived from SMOS. Note that critical studies which have investigated SMOS τ found that it was relatively noisy and Hornbuckle et al. (2016) proposed different smoothing techniques to extract a smooth temporal variation of τ from the noisy τ retrievals. ESA is currently funding studies for the development of a robust vegetation optical depth product.

The interest of accounting for the dependence of optical depth τ_P on incidence angle and polarization was confirmed in several studies over low vegetation based on tower-based or airborne observations (Fernandez-Moran et al., 2015; Peischl et al., 2012; Schwank et al., 2005; Schwank et al., 2012; Yan et al., 2015). In addition, recent studies found a differentiation between the values of ω at H- and V-polarization, especially over low vegetation covers (Kurum, 2013; Lievens et al., 2015; Saleh et al., 2007). At the scale of large footprints measured from space-borne observations, it is likely these effects are averaged out and can be neglected (Owe et al., 2001). So, to date no studies have demonstrated the need to account for the dependence of optical depth (and single scattering albedo) on polarization and incidence angle in SM retrievals at the scale of space-borne observations, with these effects generally found to be low over forests (Grant et al., 2008; Rahmoune et al., 2013). However, specific studies analyzing in detail this question from L-band satellite data are still required.

The link between optical depth at nadir (τ_{NAD}) and vegetation indices (LAI, NDVI, and VWC) has been investigated over a variety of low vegetation covers from tower-based and airborne observations at L-band. Recently, some studies on this topic have been made based on SMOS observations (Grant et al., 2016; Lawrence et al., 2014). It seems there was a convergence of results towards values of b″ close to 0.06 for low vegetation. The main issue encountered by these two studies was the fact that τ_{NAD} products derived from the SMOS observations are relatively noisy.

7.2.3. Interception & litter effects

Several experimental studies summarized here have shown that water interception by the vegetation canopy and ground litter effects may have a significant effect on TB (0). These effects are stronger in natural and/or forest environments where litter, senescent vegetation, organic substrates (especially in Northern environments) are abundant. It is likely that the effect of litter can be accounted for by (i) higher values of the H_R parameter and/or by (ii) a strong dependence of H_R on SM, as found by Saleh et al. (2007) over grassland and by Grant et al. (2008) over forests from tower-based experiments. However, there is no consensus on this question at local scale and moreover this issue has rarely been addressed by studies based on space-borne observations. We think this is also a key topic of research to improve SM retrievals derived from passive microwave satellite data.

Uncited references

Holmes et al., 2008
Konings et al., 2015
Schwank et al., 2015

Acknowledgements

This research work was funded by CNES (Centre National d'Etudes Spatiales) through the Science TOSCA (Terre Océan Surfaces Continentales et Atmosphère) program.

References

Al Bitar, A., Mialon, A., Kerr, Y., Jacquette, E., Cabot, F., Richaume, P., Quesney, A., Tarrot, S., Parrens, M., Tomer, S., Molero, B., Pellarin, T., Al-Yaari, A., Wigneron, J.P., 2016. The SMOS level 3 daily soil moisture maps using multi-orbit retrieval algorithm. Remote Sens. Environ. (submitted).

Allen, C.T., Ulaby, F.T., 1984. Modeling the polarization dependence of the attenuation in vegetation canopies. In: 1984 IEEE Int. Geosci. Remote Sensing Symp. (IGARSS'84) Dig. (Strasbourg, France, Aug. 27–30, 1984).

Al-Yaari, A., Wigneron, J.P., Ducharne, A., Kerr, Y., de Rosnay, P., de Jeu, R., Govind, A., Al Bitar, A., Albergel, C., Muñoz-Sabater, J., Richaume, P., Mialon, A., 2014. Global-scale evaluation of two satellite-based passive microwave soil moisture datasets (SMOS and AMSR-E) with respect to land data assimilation system estimates. Remote Sens. Environ. 149, 181–195.

Balsamo, G., Mahfouf, J.F., Bélair, S., Deblonde, G., 2006. A global root-zone soil moisture analysis using simulated L-band brightness temperature in preparation for the hydros satellite mission. J. Hydrometeorol. 7, 1126–1146.

Bindlish, R., Jackson, T., Cosh, M., Zhao, T., Neill, P.O., 2015. Global soil moisture from the aquarius/SAC-D satellite: description and initial assessment. IEEE Geosci. Remote Sens. Lett. 12, 923–927.

Bircher, S., Balling, J.E., Skou, N., Kerr, Y.H., 2012. Validation of SMOS brightness temperatures during the HOBE airborne campaign, western Denmark. IEEE Trans. Geosci. Remote Sens. 50, 1468–1482.

Bircher, S., Skou, N., Kerr, Y.H., 2013. Validation of SMOS L1C and L2 products and important parameters of the retrieval algorithm in the Skjern River catchment, western Denmark. IEEE Trans. Geosci. Remote Sens. 51, 2969–2985.

Bircher, S., Kerr, Y.H., Wigneron, J.-P., 2015. SMOSHiLat – Microwave L-band emissions from organic-rich soils in the northern cold climate zone and their impact on the SMOS soil moisture product. In: ESA – STSE – Changing Earth Science Network – Call 2012, ESA/ESRIN Contract 4000107338/12/I-BG, Final Report p. 71.

Bircher, S., Andreasen, M., Vuollet, J., Vehviläinen, J., Rautiainen, K., Jonard, F., Weihermüller, L., Zakharova, E., Wigneron, J.P., Kerr, Y.H., 2016. Soil moisture sensor calibration for organic soil surface layers. Geosci. Instrum. Method. Data Syst. 5, 109–125.

Bircher, S., Demontoux, F., Razafindratsima, S., Zakharova, E., Drusch, M., Wigneron, J.-P., Kerr, Y., 2017. L-band relative permittivity of organic soil surface layers – a new dataset of resonant cavity measurements and model evaluation. Remote Sens. (in press).

Broschat, S.L., 1993. The small slope approximation reflection coefficient for scattering from a “Pierson-Moskowitz” sea surface. IEEE Trans. Geosci. Remote Sens. 31, 1112–1114.

Cano, A., Saleh, K., Wigneron, J.-P., Antolín, C., Balling, J.E., Kerr, Y.H., Kruszewski, A., Millán-Scheiding, C., Søbjærg, S.S., Skou, N., López-Baeza, E., 2010. The SMOS Mediterranean Ecosystem L-Band Characterisation EXperiment (MELBEX-I) over natural shrubs. Remote Sens. Environ. 114, 844–853.

Carrera, M.L., Bélair, S., Bilodeau, B., 2015. The Canadian Land Data Assimilation System (CaLDAS): description and synthetic evaluation study. J. Hydrometeorol. 16, 1293–1314.

Chan, S., Bindlish, R., O'Neill, P., Njoku, E., Jackson, T., Colliander, A., et al., 2016. Assessment of the SMAP passive soil moisture product. IEEE Trans. Geosci. Remote Sens. 54, 1–14.

Channan, S., Collins, K., Emanuel, W.R., 2014. Global Mosaics of the Standard MODIS Land Cover Type Data. University of Maryland and the Pacific Northwest National Laboratory, College Park, Maryland, USA.

Choudhury, B.J., Schmugge, T.J., Chang, A., Newton, R.W., 1979. Effect of surface roughness on the microwave emission from soils. Journal of Geophysical Research: Oceans 84, 5699–5706.

Choudhury, B.J., Schmugge, T.J., Mo, T., 1982. A parameterization of effective soil temperature for microwave emission. Journal of Geophysical Research: Oceans 87, 1301–1304.

Crow, W.T., Wood, E.F., 2003. The assimilation of remotely sensed soil brightness temperature imagery into a land surface model using ensemble Kalman filtering: a case study based on ESTAR measurements during SGP97. Adv. Water Resour. 26, 137–149.

Davenport, I.J., Fernandez-Galvez, J., Gurney, R.J., 2005. A sensitivity analysis of soil moisture retrieval from the tau-omega microwave emission model. IEEE Trans. Geosci. Remote Sens. 43, 1304–1316.

De Jeu, R.A.M., Wagner, W., Holmes, T.R.H., Dolman, A.J., Van de Giesen, N.C., Friesen, J., 2008. Global soil moisture patterns observed by space bornemicrowave radiometers and scatterometers. Surv. Geophys. 29, 399–420. http://dx.doi.org/10.1007/s10712-008-9044-0.

De Jeu, R.A.M., Holmes, T.R.H., Panciera, R., Walker, J.P., 2009. Parameterization of the land parameter retrieval model for L-band observations using the NAFE'05 data set. IEEE Geosci. Remote Sens. Lett. 6, 630–634.

De Lannoy, G.J.M., Reichle, R.H., 2016. Assimilation of SMOS brightness temperatures or soil moisture retrievals into a land surface model. Hydrol. Earth Syst. Sci. http://dx.doi.org/10.5194/hess-2016-414.

De Lannoy, G.J.M., Reichle, R.H., 2015. Global assimilation of multiangle and multipolarization SMOS brightness temperature observations into the GEOS-5 catchment land surface model for soil moisture estimation. J. Hydrometeorol. 17, 669–691.

De Lannoy, G.J.M., Reichle, R.H., Pauwels, V.R.N., 2013. Global calibration of the GEOS-5 L-band microwave radiative transfer model over nonfrozen land using SMOS observations. J. Hydrometeorol. 14, 765–785.

De Lannoy, G.J.M., Reichle, R.H., Vrugt, J.A., 2014. Uncertainty quantification of GEOS-5 L-band radiative transfer model parameters using Bayesian inference and SMOS observations. Remote Sens. Environ. 148, 146–157.

Della Vecchia, A.D., Ferrazzoli, P., Guerriero, L., Rahmoune, R., Paloscia, S., Pettinato, S., Santi, E., 2010. Modeling the multifrequency emission of broadleaf forests and their components. IEEE Trans. Geosci. Remote Sens. 48, 260–272.

Demontoux, F., Le Crom, B., Ruffié, G., Wigneron, J.P., Grant, J.P., Mironov, V.L., Lawrence, H., 2008. Electromagnetic characterization of soil-like media: application to the simulation of the microwave emissivity of the ground surface in forests. The European Physical Journal - Applied Physics 44, 213–219.

Dobson, M.C., Ulaby, F.T., Hallikainen, M.T., El-Rayes, M.A., 1985. Microwave dielectric behavior of wet soil-part II: dielectric mixing models. Geoscience and Remote Sensing, IEEE Transactions on GE-23, 35–46.

Du, J., Kimball, J.S., Jones, L.A., 2016. Passive microwave remote sensing of soil moisture based on dynamic vegetation scattering properties for AMSR-E. IEEE Trans. Geosci. Remote Sens. 54, 597–608.

Entekhabi, D., Nakamura, H., Njoku, E.G., 1994. Solving the inverse problem for soil moisture and temperature profiles by sequential assimilation of multifrequency remotely sensed observations. IEEE Trans. Geosci. Remote Sens. 32, 438–448.

Entekhabi, D., Njoku, E.G., O'Neill, P.E., Kellogg, K.H., Crow, W.T., Edelstein, W.N., Entin, J.K., Goodman, S.D., Jackson, T.J., Johnson, J., Kimball, J., Piepmeier, J.R., Koster, R.D., Martin, N., McDonald, K.C., Moghaddam, M., Moran, S., Reichle, R., Shi, J.C., Spencer, M.W., Thurman, S.W., Leung, T. & Van Zyl, J. (2010). The Soil Moisture Active Passive (SMAP) mission. Proc. IEEE, 98, 704–716

Entekhabi, D., Yueh, S., O'Neill, P., Kellogg, K.A.C.-A., 2014. SMAP Handbook. JPL Publication JPL 400–1567. Jet Propulsion Laboratory, Pasadena, California, 182.

Escorihuela, M.J., Kerr, Y.H., Rosnay, P.d., Wigneron, J.P., Calvet, J.C., Lemaitre, F., 2007. A simple model of the bare soil microwave emission at L-band. IEEE Trans. Geosci. Remote Sens. 45, 1978–1987.

Escorihuela, M.J., Chanzy, A., Wigneron, J.P., Kerr, Y.H., 2010. Effective soil moisture sampling depth of L-band radiometry: a case study. Remote Sens. Environ. 114, 995–1001.

Fernandez-Moran, R., Wigneron, J.P., Lopez-Baeza, E., Al-Yaari, A., Coll-Pajaron, A., Mialon, A., Miernecki, M., Parrens, M., Salgado-Hernanz, P.M., Schwank, M., Wang, S., Kerr, Y.H., 2015. Roughness and vegetation parameterizations at L-band for soil moisture retrievals over a vineyard field. Remote Sens. Environ. 170, 269–279.

Fernandez-Moran, R., Wigneron, J.-P., Lopez-Baeza, E., Mialon, A., Parrens, M., Al Bitar, A., Richaume, P., Kerr, Y., 2016. Evaluation of Soil Moisture Retrievals at L-band Under Different Assumptions Over Several Regions of the Globe. IGARSS 2016, Beijing, China (July 10–15).

Ferrazzoli, P., Guerriero, L., 1996. Passive microwave remote sensing of forests: a model investigation. IEEE Trans. Geosci. Remote Sens. 34, 433–443.

Ferrazzoli, P., Guerriero, L., Wigneron, J.-P., 2002. Simulating L-band emission of forests in view of future satellite applications. Geoscience and Remote Sensing, IEEE Transactions on 40, 2700–2708.

Fung, A.K., 1994. Microwave Scattering and Emission Models and Their Applications. Artech House, Norwood, MA.

Galantowicz, J.F., Entekhabi, D., Njoku, E.G., 1999. Tests of sequential data assimilation for retrieving profile soil moisture and temperature from observed L-band radiobrightness. IEEE Trans. Geosci. Remote Sens. 37, 1860–1870.

Gao, Y., Walker, J.P., Kerr, Y., Monerris, A., 2013. Intercomparison of Surface Roughness Parameterizations for Soil Moisture Retrieval. IEEE International Geoscience and Remote Sensing Symposium (IGARSS), Melbourne, Australia (21–26 July, 2013).

Gao, Y., Walker, J.P., Allahmoradi, M., Monerris, A., Ryu, D., Jackson, T.J., 2015. Optical sensing of vegetation water content: a synthesis study. IEEE Journal of Selected Topics in Applied Earth Observations and Remote Sensing 8, 1456–1464.

Grant, J.P., Wigneron, J.P., Van de Griend, A.A., Kruszewski, A., Søbjærg, S.S., Skou, N., 2007. A field experiment on microwave forest radiometry: L-band signal behaviour for varying conditions of surface wetness. Remote Sens. Environ. 109, 10–19.

Grant, J.P., Saleh-Contell, K., Wigneron, J.P., Guglielmetti, M., Kerr, Y.H., Schwank, M., Skou, N., Griend, A.A.V.D., 2008. Calibration of the L-MEB model over a coniferous and a deciduous forest. IEEE Trans. Geosci. Remote Sens. 46, 808–818.

Grant, J.P., Griend, A.A.V.D., Schwank, M., Wigneron, J.P., 2009. Observations and modeling of a pine forest floor at L-band. IEEE Trans. Geosci. Remote Sens. 47, 2024–2034.

Grant, J.P., Wigneron, J.P., De Jeu, R.A.M., Lawrence, H., Mialon, A., Richaume, P., Al Bitar, A., Drusch, M., van Marle, M.J.E., Kerr, Y., 2016. Comparison of SMOS and AMSR-E vegetation optical depth to four MODIS-based vegetation indices. Remote Sens. Environ. 172, 87–100.

Guglielmetti, M., Schwank, M., Mätzler, C., Oberdörster, C., Vanderborght, J., Flühler, H., 2007. Measured microwave radiative transfer properties of a deciduous forest canopy. Remote Sens. Environ. 109, 523–532.

Guglielmetti, M., Schwank, M., Matzler, C., Oberdorster, C., Vanderborght, J., Fluhler, H., 2008. FOSMEX: forest soil moisture experiments with microwave radiometry. IEEE Trans. Geosci. Remote Sens. 46, 727–735.

Holmes, T.R.H., Drusch, M., Wigneron, J.-P., De Jeu, R.A.M., 2008. A global simulation of microwave emission: error structures based on output from ECMWF's operational integrated forecast system. IEEE Trans. Geosci. Remote Sens. 46 (3), 846–856. http://dx.doi.org/10.1109/TGRS.2007.914798.

Holmes, T.R.H., de Rosnay, P., de Jeu, R., Wigneron, R.J.P., Kerr, Y., Calvet, J.C., Escorihuela, M.J., Saleh, K., Lemaître, F., 2006. A new parameterization of the effective temperature for L band radiometry. Geophys. Res. Lett. 33, (n/a–n/a).

Hornbuckle, B.K., England, A.W., Anderson, M.C., Viner, B.J., 2006. The effect of free water in a maize canopy on microwave emission at 1.4 GHz. Agric. For. Meteorol. 138, 180–191.

Hornbuckle, B.K., Patton, J.C., VanLoocke, A., Suyker, A.E., Roby, M.C., Walker, V.A., Iyer, E.R., Herzmann, D.E., Endacott, E.A., 2016. SMOS optical thickness changes in response to the growth and development of crops, crop management, and weather. Remote Sens. Environ. 180, 320–333.

Huang, S., Tsang, L., Njoku, E.G., Chan, K.S., 2010. Backscattering coefficients, coherent reflectivities, and emissivities of randomly rough soil surfaces at L-band for SMAP applications based on numerical solutions of Maxwell equations in three-dimensional simulations. IEEE Trans. Geosci. Remote Sens. 48, 2557–2568.

Jackson, T., O'Neill, P., Njoku, E., Chan, S., Bindlish, R., Colliander, A., Chen, F., Burgin, M., Dunbar, S., Piepmeier, J., Cosh, M., Caldwell, T., Walker, J., Wu, X.,

Berg, A., Rowlandson, T., Pacheco, A., McNairn, H., Thibeault, M., Martínez-Fernández, J., González-Zamora, , Seyfried, M., Bosch, D., Starks, P., Goodrich, D., Prueger, J., Su, Z., van der Velde, R., Asanuma, J., Palecki, M., Small, E., Zreda, M., Calvet, J., Crow, W., Kerr, Y., Yueh, S., Entekhabi, D., 2016. Calibration and Validation for the L2/3_SM_P Version 3 Data Products, SMAP Project, JPL D-93720. Jet Propulsion Laboratory, Pasadena, CA.

Jackson, T.J., 1993. III. Measuring surface soil moisture using passive microwave remote sensing. Hydrol. Process. 7, 139–152.

Jackson, T.J., Schmugge, T.J., 1991. Vegetation effects on the microwave emission of soils. Remote Sens. Environ. 36, 203–212.

Jackson, T.J., Gasiewski, A.J., Oldak, A., Klein, M., Njoku, E.G., Yevgrafov, A., Christiani, S., Bindlish, R., 2002. Soil moisture retrieval using the C-band polarimetric scanning radiometer during the Southern Great Plains 1999 experiment. IEEE Trans. Geosci. Remote Sens. 40, 2151–2161.

Jackson, T.J., Chen, D., Cosh, M., Li, F., Anderson, M., Walthall, C., Doriaswamy, P., Hunt, E.R., 2004. Vegetation water content mapping using Landsat data derived normalized difference water index for corn and soybeans. Remote Sens. Environ. 92, 475–482.

Jackson, T.J., Cosh, M.H., Bindlish, R., Starks, P.J., Bosch, D.D., Seyfried, M., Goodrich, D.C., Moran, M.S., Jinyang, D., 2010. Validation of advanced microwave scanning radiometer soil moisture products. Geoscience and Remote Sensing, IEEE Transactions on 48, 4256–4272.

Jones, M.O., Jones, L.A., Kimball, J.S., McDonald, K.C., 2011. Satellite passive microwave remote sensing for monitoring global land surface phenology. Remote Sens. Environ. 115, 1102–1114.

Jones, S.B., Wraith, J.M., Or, D., 2002. Time domain reflectometry measurement principles and applications. Hydrol. Process. 16, 141–153.

Joseph, J.H., Wiscombe, W.J., Weinman, J.A., 1976. The Delta-Eddington approximation for radiative flux transfer. J. Atmos. Sci. 33, 2452–2459.

Karam, M.A., 1997. A physical model for microwave radiometry of vegetation. IEEE Trans. Geosci. Remote Sens. 35, 1045–1058.

Kellner, E., Lundin, L.-C., 2001. Calibration of time domain reflectometry for water content in peat soil. Hydrol. Res. 32, 315–332.

Kerr, Y.H., Njoku, E.G., 1990. A semiempirical model for interpreting microwave emission from semiarid land surfaces as seen from space. Geoscience and Remote Sensing, IEEE Transactions on 28, 384–393.

Kerr, Y.H., Waldteufel, P., Wigneron, J.P., Martinuzzi, J., Font, J., Berger, M., 2001. Soil moisture retrieval from space: the Soil Moisture and Ocean Salinity (SMOS) mission. Geoscience and Remote Sensing, IEEE Transactions on 39, 1729–1735.

Kerr, Y.H., Waldteufel, P., Wigneron, J.P., Delwart, S., Cabot, F., Boutin, J., Escorihuela, M.J., Font, J., Reul, N., Gruhier, C., Juglea, S.E., Drinkwater, M.R., Hahne, A., Martin-Neira, M., Mecklenburg, S., 2010. The SMOS mission: new tool for monitoring key elements ofthe global water cycle. Proc. IEEE 98, 666–687.

Kerr, Y.H., Waldteufel, P., Richaume, P., Wigneron, J.P., Ferrazzoli, P., Mahmoodi, A., Al Bitar, A., Cabot, F., Gruhier, C., Juglea, S.E., Leroux, D., Mialon, A., Delwart, S., 2012. The SMOS soil moisture retrieval algorithm. Geoscience and Remote Sensing, IEEE Transactions on 50, 1384–1403.

Kerr, Y.H., Waldteufel, P., Richaume, P., Ferrazzoli, P., Wigneron, J.-P., 2014. SMOS level 2 processor Soil Moisture Algorithm Theoretical Basis Document (ATBD) V4.a In (142 p.). SM-ESL (CBSA), Toulouse.

Kerr, Y.H., Al-Yaari, A., Rodriguez-Fernandez, N., Parrens, M., Molero, B., Leroux, D., Bircher, S., Mahmoodi, A., Mialon, A., Richaume, P., Delwart, S., Al Bitar, A., Pellarin, T., Bindlish, R., Jackson, T.J., Rudiger, C., Waldteufel, P., Mecklenburg, S., Wigneron, J.-P., 2016. Overview of SMOS performance in terms of global soil moisture monitoring after six years in operation. Remote Sens. Environ. 180, 40–63.

Konings, A., Gentine, P., 2016. Global variations in ecosystem-scale isohydricity. Glob. Chang. Biol.http://dx.doi.org/10.1111/gcb.13389.

Konings, A.G., McColl, K.A., Piles, M., Entekhabi, D., 2015. How many parameters can be maximally estimated from a set of measurements? IEEE Trans. Geosci. Remote Sens. Lett. 12, 1081–1085.

Konings, A.G., Piles, M., Rötzer, K., McColl, K.A., Chan, S.K., Entekhabi, D., 2016. Vegetation optical depth and scattering albedo retrieval using time series of dual-polarized L-band radiometer observations. Remote Sens. Environ. 172, 178–189.

Kurum, M., 2013. Quantifying scattering albedo in microwave emission of vegetated terrain. Remote Sens. Environ. 129, 66–74.

Kurum, M., Lang, R.H., Neill, P.E.O., Joseph, A.T., Jackson, T.J., Cosh, M.H., 2011. A first-order radiative transfer model for microwave radiometry of forest canopies at L-band. IEEE Trans. Geosci. Remote Sens. 49, 3167–3179.

Kurum, M., O'Neill, P.E., Lang, R.H., Joseph, A.T., Cosh, M.H., Jackson, T.J., 2012. Effective tree scattering and opacity at L-band. Remote Sens. Environ. 118, 1–9.

Lawrence, H., Demontoux, F., Wigneron, J.P., Paillou, P., Wu, T.D., Kerr, Y.H., 2011. Evaluation of a numerical modeling approach based on the finite-element method for calculating the rough surface scattering and emission of a soil layer. IEEE Geosci. Remote Sens. Lett. 8, 953–957.

Lawrence, H., Wigneron, J.P., Demontoux, F., Mialon, A., Kerr, Y.H., 2013. Evaluating the semiempirical H–Q model used to calculate the L-band emissivity of a rough bare soil. IEEE Trans. Geosci. Remote Sens. 51, 4075–4084.

Lawrence, H., Wigneron, J.-P., Richaume, P., Novello, N., Grant, J., Mialon, A., Al Bitar, A., Merlin, O., Guyon, D., Leroux, D., Bircher, S., Kerr, Y., 2014. Comparison between SMOS vegetation optical depth products and MODIS vegetation indices over crop zones of the USA. Remote Sens. Environ. 140, 396–406.

Le Vine, D.M., Lagerloef, G.S.E., Torrusio, S.E., 2010. Aquarius and remote sensing of sea surface salinity from space. Proc. IEEE 98, 688–703.

Lemmetyinen, J., Schwank, M., Rautiainen, K., Kontu, A., Parkkinen, T., Mätzler, C., Wiesmann, A., Wegmüller, U., Derksen, C., Toose, P., Roy, A., Pulliainen, J., 2016. Snow density and ground permittivity retrieved from L-band radiometry: application to experimental data. Remote Sens. Environ. 180, 377–391.

Li, H., Parent, L.E., Karam, A., Tremblay, C., 2004. Potential of sphagnum peat for improving soil organic matter, water holding capacity, bulk density and potato yield in a sandy soil. Plant Soil 265, 355–365.

Lievens, H., Al Bitar, A., Verhoest, N.E.C., Cabot, F., De Lannoy, G.J.M., Drusch, M., Dumedah, G., Hendricks Franssen, H.J., Kerr, Y., Tomer, S.K., Martens, B., Merlin, O., Pan, M., van den Berg, M.J., Vreeckem, H., Walker, J.P., Wood, E.F., Pauwels, V.R.N., 2015. Optimization of a radiative transfer forward operator for simulating SMOS brightness temperatures over the Upper Mississippi Basin. J. Hydrometeorol. 16, 1109–1134.

Liu, Y.Y., Dijk, A.I., McCabe, M.F., Evans, J.P., De Jeu, R.A.M., 2013. Global vegetation biomass change (1988–2008) and attribution to environmental and human drivers. Glob. Ecol. Biogeogr. 22 (6), 692–705.

Liu, Y.Y., van Dijk, A.I., De Jeu, R.A.M., Canadell, J.G., McCabe, M.F., Evans, J.P., Wang, G., 2015. Recent reversal in loss of global terrestrial biomass. Nat. Clim. Chang. 5, 470–474.

Liu, Y.Y., de Jeu, R.A.M., McCabe, M.F., Evans, J.P., van Dijk, A.I.J.M., 2011. Global long-term passive microwave satellite-based retrievals of vegetation optical depth. Geophys. Res. Lett. 38 (n/a–n/a).

Lv, S., Wen, J., Zeng, Y., Tian, H., Su, Z., 2014. An improved two-layer algorithm for estimating effective soil temperature in microwave radiometry using in situ temperature and soil moisture measurements. Remote Sens. Environ. 152, 356–363.

Macelloni, G., Paloscia, S., Pampaloni, P., Ruisi, R., 2001. Airborne multifrequency L- to Ka-band radiometric measurements over forests. IEEE Trans. Geosci. Remote Sens. 39, 2507–2513.

Martens, B., Lievens, H., Colliander, A., Jackson, T.J., Verhoest, N.E.C., 2015. Estimating effective roughness parameters of the L-MEB model for soil moisture retrieval using passive microwave observations from SMAPVEX12. IEEE Trans. Geosci. Remote Sens. 53, 4091–4103.

Mätzler, C., 1998. Microwave permittivity of dry sand. IEEE Trans. Geosci. Remote Sens. 36, 317–319.

Mätzler, C., Rosenkranz, P.W., Battaglia, A., Wigneron, J.-P., 2006. Thermal microwave radiation - applications for remote sensing. In: IET Electromagnetic Waves Series 52. UK, London, p. 555.

Mecklenburg, S., Drusch, M., Kaleschke, L., Rodriguez-Fernandez, N., Reul, N., et al., 2016. ESA's soil moisture and ocean salinity mission: from science to operational applications. Remote Sens. Environ. 180, 3–18.

Merlin, O., Walker, J.P., Panciera, R., Escorihuela, M.J., Jackson, T.J., 2009. Assessing the SMOS soil moisture retrieval parameters with high-resolution NAFE'06 data. IEEE Geosci. Remote Sens. Lett. 6, 635–639.

Mialon, A., Coret, L., Kerr, Y.H., Sécherre, F., Wigneron, J.-P., 2008. Flagging the topographic impact on the SMOS signal. IEEE Trans. Geosci. Remote Sens. 46 (3), 689–694.

Mialon, A., Wigneron, J.P., Rosnay, P.D., Escorihuela, M.J., Kerr, Y.H., 2012. Evaluating the L-MEB model from long-term microwave measurements over a rough field, SMOSREX 2006. IEEE Trans. Geosci. Remote Sens. 50, 1458–1467.

Mialon, A., Richaume, P., Leroux, D., Bircher, S., Al Bitar, A., Pellarin, T., Wigneron, J.P., Kerr, Y.H., 2015. Comparison of Dobson and Mironov dielectric models in the SMOS soil moisture retrieval algorithm. IEEE Trans. Geosci. Remote Sens. 53, 3084–3094.

Mironov, V., Savin, I., 2015. A temperature-dependent multi-relaxation spectroscopic dielectric model for thawed and frozen organic soil at 0.05–15 GHz. Phys. Chem. Earth, Parts A/B/C 83–84, 57–64.

Mironov, V., Kerr, Y., Wigneron, J.P., Kosolapova, L., Demontoux, F., 2012. Temperature- and texture-dependent dielectric model for moist soils at 1.4 GHz. IEEE Geosci. Remote Sens. Lett. 10, 419–423.

Mironov, V., Kerr, Y., Wigneron, J.P., Kosolapova, L., Demontoux, F., 2013. Temperature and texture dependent dielectric model for moist soils at 1.4 GHz. IEEE Geosci. Remote Sens. Lett. 10, 419–423.

Mironov, V.L., Fomin, S.V., 2009. Temperature and Mineralogy Dependable Model for Microwave Dielectric Spectra of Moist Soils. PIERS Proceeding, August 18–21, Moscow RUSSIA, 938–942.

Mironov, V.L., Fomin, S.V., 2009. Temperature Dependable Microwave Dielectric Model for Moist Soils. PIERS Proceedings, March 23–27, Beijing CHINA, 831–835.

Mironov, V.L., Lukin, Y.I., 2011. A physical model of dielectric spectra of thawed and frozen bentonitic clay within the frequency range from 1 to 15 GHZ. Russ. Phys. J. 53, 956–963.
Mironov, V.L., Dobson, M.C., Kaupp, V.H., Komarov, S.A., Kleshchenko, V.N., 2004. Generalized refractive mixing dielectric model for moist soils. IEEE Trans. Geosci. Remote Sens. 42, 773–785.
Mironov, V.L., Kosolapova, L.G., Fomin, S.V., 2009. Physically and mineralogically based spectroscopic dielectric model for moist soils. Geoscience and Remote Sensing, IEEE Transactions on 47, 2059–2070.
Mironov, V.L., Roo, R.D.D., Savin, I.V., 2010. Temperature-dependable microwave dielectric model for an Arctic soil. IEEE Trans. Geosci. Remote Sens. 48, 2544–2556.
Mironov, V.L., Bobrov, P.P., Fomin, S.V., 2013. Multirelaxation generalized refractive mixing dielectric model of moist soils. IEEE Geosci. Remote Sens. Lett. 10, 603–606.
Mironov, V.L., Bobrov, P.P., Fomin, S.V., Karavaiskii, A.Y., 2013. Generalized refractive mixing dielectric model of moist soils considering ionic relaxation of soil water. Russ. Phys. J. 56, 319–324.
Mo, T., Schmugge, T.J., 1987. A parameterization of the effect of surface roughness on microwave emission. IEEE Trans. Geosci. Remote Sens. GE-25, 481–486.
Mo, T., Choudhury, B.J., Schmugge, T.J., Wang, J.R., Jackson, T.J., 1982. A model for microwave emission from vegetation-covered fields. Journal of Geophysical Research: Oceans 87, 11229–11237.
Monerris, A., Benedicto, P., Vall-llossera, M., Camps, A., Santanach, E., Piles, M., Prehn, R., 2008. Assessment of the topography impact on microwave radiometry at L-band. J. Geophys. Res. 113, B12.
Montpetit, B., Royer, A., Wigneron, J.P., Chanzy, A., Mialon, A., 2015. Evaluation of multi-frequency bare soil microwave reflectivity models. Remote Sens. Environ. 162, 186–195.
Muñoz-Sabater, J., 2015. Incorporation of passive microwave brightness temperatures in the ECMWF soil moisture analysis. Remote Sens. 7, 5758–5784.
Muñoz-Sabater, J., de Rosnay, P., Balsamo, G., 2011. Sensitivity of L-band NWP forward modelling to soil roughness. Int. J. Remote Sens. 32 (19), 5607–5620.
Muñoz-Sabater, J., Fouilloux, A., Rosnay, P.d., 2012. Technical implementation of SMOS data in the ECMWF integrated forecasting system. IEEE Geosci. Remote Sens. Lett. 9, 252–256.
Njoku, E.G., Chan, S.K., 2006. Vegetation and surface roughness effects on AMSR-E land observations. Remote Sens. Environ. 100, 190–199.
Oh, Y., Kay, Y.C., 1998. Condition for precise measurement of soil surface roughness. IEEE Trans. Geosc. Remote Sens. 36 (2), 691–695.
O'Neill, P., S. Chan, E. Njoku, T. Jackson & Bindlish, R. (2015). "Algorithm Theoretical Basis Document (ATBD): L2/3_SM_P," Initial Release, v.3, October 1, 2015. Available at http://smap.jpl.nasa.gov/science/dataproducts/ATBD/
Owe, M., de Jeu, R., Walker, J., 2001. A methodology for surface soil moisture and vegetation optical depth retrieval using the microwave polarization difference index. IEEE Trans. Geosci. Remote Sens. 39, 1643–1654.
Panciera, R., Walker, J.P., Kalma, J.D., Kim, E.J., Saleh, K., Wigneron, J.-P., 2009. Evaluation of the SMOS L-MEB passive microwave soil moisture retrieval algorithm. Remote Sens. Environ. 113, 435–444.
Panciera, R., Walker, J.P., Merlin, O., 2009. Improved understanding of soil surface roughness parameterization for L-band passive microwave soil moisture retrieval. IEEE Geosci. Remote Sens. Lett. 6, 625–629.
Panciera, R., Walker, J.P., Jackson, T.J., Gray, D.A., Tanase, M.A., Ryu, D., Monerris, A., Yardley, H., Rudiger, C., Wu, X., Gao, Y., Hacker, J.M., 2014. The soil moisture active passive experiments (SMAPEx): toward soil moisture retrieval from the SMAP mission. IEEE Trans. Geosci. Remote Sens. 52, 490–507.
Pardé, M., Wigneron, J.P., Waldteufel, P., Kerr, Y.H., Chanzy, A., Sobjaerg, S.S., Skou, N., 2004. N-parameter retrievals from L-band microwave observations acquired over a variety of crop fields. IEEE Trans. Geosci. Remote Sens. 42, 1168–1178.
Pardé, M., Zribi, M., Wigneron, J.-P., Dechambre, M., Fanise, P., Kerr, Y., Crapeau, M., Saleh, K., Calvet, J.-C., Albergel, C., Mialon, A., Novello, N., 2011. Soil moisture estimations based on airborne CAROLS L-band microwave data. Remote Sens. 3.
Parrens, M., Wigneron, J.-P., Richaume, P., Mialon, A., Al Bitar, A., Fernandez-Moran, R., Al-Yaari, A., Kerr, Y.H., 2016. Global-scale surface roughness effects at L-band as estimated from SMOS observations. Remote Sens. Environ. 181, 122–136.
Parrens, M., Wigneron, J.-P., Richaume, P., Al Bitar, A., Mialon, A., Fernandez-Moran, R., Alyaari, A., O'Neill, P., Kerr, Y., 2017. Considering combined or separated roughness and vegetation effects in soil moisture retrievals. Int. J. Appl. Earth Obs. Geoinf. 55, 73–86.
Patton, J., Hornbuckle, B., 2013. Initial validation of SMOS vegetation optical thickness in Iowa. IEEE Geosci. Remote Sens. Lett. 10, 647–651.
Peake, W., 1959. Interaction of electromagnetic waves with some natural surfaces. IRE Transactions on Antennas and Propagation 7, 324–329.
Peischl, S., Walker, J.P., Ryu, D., Kerr, Y.H., Panciera, R., Rudiger, C., 2012. Wheat canopy structure and surface roughness effects on multiangle observations at L-band. IEEE Trans. Geosci. Remote Sens. 50, 1498–1506.
Peischl, S., Walker, J.P., Ye, N., Ryu, D., Kerr, Y., 2014. Sensitivity of multi-parameter soil moisture retrievals to incidence angle configuration. Remote Sens. Environ. 143, 64–72.
Pellarin, T., Calvet, J.C., Wigneron, J.P., 2003. Surface soil moisture retrieval from L-band radiometry: a global regression study. Geoscience and Remote Sensing, IEEE Transactions on 41, 2037–2051.
Pellarin, T., Kerr, Y.H., Wigneron, J.P., 2006. Global simulation of brightness temperatures at 6.6 and 10.7 GHz over land based on SMMR data set analysis. IEEE Trans. Geosci. Remote Sens. 44, 2492–2505.
Peplinski, N.R., Ulaby, F.T., Dobson, M.C., 1995. Dielectric properties of soils in the 0.3–1.3-GHz range. IEEE Trans. Geosci. Remote Sens. 33, 803–807.
Rahmoune, R., Ferrazzoli, P., Kerr, Y., Richaume, P., 2013. SMOS level 2 retrieval algorithm over forests: description and generation of global maps. IEEE Journal of Selected Topics in Applied Earth Observations and Remote Sensing 6, 1430–1439.
Rahmoune, R., Ferrazzoli, P., Singh, Y.K., Kerr, Y.H., Richaume, P., Bitar, A.A., 2014. SMOS retrieval results over forests: comparisons with independent measurements. IEEE Journal of Selected Topics in Applied Earth Observations and Remote Sensing 7, 3858–3866.
Raju, S., Chanzy, A., Wigneron, J.-P., Calvet, J.-C., Kerr, Y., Laguerre, L., 1995. Soil moisture and temperature profile effects on microwave emission at low frequencies. Remote Sens. Environ. 54, 85–97.
Reichle, R.H., Entekhabi, D., McLaughlin, D.B., 2001. Downscaling of radio brightness measurements for soil moisture estimation: A four-dimensional variational data assimilation approach. Water Resour. Res. 37, 2353–2364.
Reichle, R.H., De Lannoy, G.J.M., Liu, Q., Colliander, A., Conaty, A., Jackson, T., Kimball, J., Koster, R.D., 2015. Soil Moisture Active Passive (SMAP) Project Assessment Report for the Beta-Release L4_SM Data Product, NASA Technical Report Series on Global Modeling and Data Assimilation. NASA/TM-2015-104606, Vol. 40. National Aeronautics and Space Administration, Goddard Space Flight Center, Greenbelt, Maryland, USA, 63.
de Rosnay, P., Calvet, J.-C., Kerr, Y., Wigneron, J.-P., Lemaître, F., Escorihuela, M.J., Sabater, J.M., Saleh, K., Barrié, J., Bouhours, G., Coret, L., Cherel, G., Dedieu, G., Durbe, R., Fritz, N.E.D., Froissard, F., Hoedjes, J., Kruszewski, A., Lavenu, F., Suquia, D., Waldteufel, P., 2006. SMOSREX: a long term field campaign experiment for soil moisture and land surface processes remote sensing. Remote Sens. Environ. 102, 377–389.
de Rosnay, P., Drusch, M., Boone, A., Balsamo, G., Decharme, B., Harris, P., Kerr, Y., Pellarin, T., Polcher, J., Wigneron, J.P., 2009. AMMA land surface model intercomparison experiment coupled to the community microwave emission model: AMMA-MEM. J. Geophys. Res. Atmos. 114, D05108.
de Rosnay, P., Muñoz Sabater, J., Drusch, M., Albergel, C., Balsamo, G., Boussetta, S., Isaksen, L., Thépaut, J.-N., 2013. Bias Correction for SMOS Data Assimilation in the ECMWF Numerical Weather Prediction System, ESA Living Planet Symposium. (Edinburgh, 09–13 September).
Roy, A., Royer, A., Wigneron, J.-P., Langlois, A., Bergeron, J., Cliche, P., 2012. A simple parameterization for a boreal forest radiative transfer model at microwave frequencies. Remote Sens. Environ. 124, 371–383.
Saleh, K., Wigneron, J.-P., de Rosnay, P., Calvet, J.-C., Kerr, Y., 2006. Semi-empirical regressions at L-band applied to surface soil moisture retrievals over grass. Remote Sens. Environ. 101, 415–426.
Saleh, K., Wigneron, J.P., Waldteufel, P., de Rosnay, P., Schwank, M., Calvet, J.C., Kerr, Y.H., 2007. Estimates of surface soil moisture under grass covers using L-band radiometry. Remote Sens. Environ. 109, 42–53.
Saleh, K., Kerr, Y.H., Richaume, P., Escorihuela, M.J., Panciera, R., Delwart, S., Boulet, G., Maisongrande, P., Walker, J.P., Wursteisen, P., Wigneron, J.P., 2009. Soil moisture retrievals at L-band using a two-step inversion approach (COSMOS/NAFE'05 experiment). Remote Sens. Environ. 113, 1304–1312.
Santi, E., Paloscia, S., Pampaloni, P., Pettinato, S., 2009. Ground-based microwave investigations of forest plots in Italy. IEEE Trans. Geosci. Remote Sens. 47, 3016–3025.
Schlenz, F., Fallmann, J., Marzahn, P., Loew, A., Mauser, W., 2012. Characterization of rape field microwave emission and implications to surface soil moisture retrievals. Remote Sens. 4.
Schmugge, T., Jackson, T.J., Kustas, W.P., Wang, J.R., 1992. Passive microwave remote sensing of soil moisture: results from HAPEX, FIFE and MONSOON 90. ISPRS J. Photogramm. Remote Sens. 47, 127–143.
Schneeberger, K., Schwank, M., Stamm, C., de Rosnay, P., Mätzler, C., Flühler, H., 2004. Topsoil structure influencing soil water retrieval by microwave radiometry. Vadose Zone J. 3, 1169–1179.
Schwank, M., Mätzler, C., 2006. Air-to-soil transition model. In: Mätzler, C., et al. (Eds.), Thermal Microwave Radiation - Applications for Remote Sensing. IET Electromagnetic Waves Series 52.

Schwank, M., Matzler, C., Guglielmetti, M., Fluhler, H., 2005. L-band radiometer measurements of soil water under growing clover grass. IEEE Trans. Geosci. Remote Sens. 43, 2225–2237.
Schwank, M., Guglielmetti, M., Matzler, C., Fluhler, H., 2008. Testing a new model for the L-band radiation of moist leaf litter. IEEE Trans. Geosci. Remote Sens. 46, 1982–1994.
Schwank, M., Völksch, I., Wigneron, J.-P., Kerr, Y.H., Mialon, A., de Rosnay, P., Mätzler, C., 2010. Comparison of two bare-soil reflectivity models and validation with L-band radiometer measurements. IEEE Trans. Geosci. Remote Sens. 48, 1.
Schwank, M., Wigneron, J.P., Lopez-Baeza, E., Volksch, I., Matzler, C., Kerr, Y.H., 2012. L-band radiative properties of vine vegetation at the MELBEX III SMOS Cal/Val site. IEEE Trans. Geosci. Remote Sens. 50, 1587–1601.
Schwank, M., Mätzler, C., Wiesmann, A., Wegmüller, U., Pulliainen, J., Lemmetyinen, J., Rautiainen, K., Derksen, C., Toose, P., Drusch, M., 2015. Snow density and ground permittivity retrieved from L-band radiometry: a synthetic analysis. IEEE Journal of Selected Topics in Applied Earth Observations and Remote Sensing 8, 3833–3845.
Shi, J., Chen, K.S., Qin, L., Jackson, T.J., Neill, P.E.O., Leung, T., 2002. A parameterized surface reflectivity model and estimation of bare-surface soil moisture with L-band radiometer. IEEE Trans. Geosci. Remote Sens. 40, 2674–2686.
Srivastava, P.K., O'Neill, P., Cosh, M., Kurum, M., Lang, R., Joseph, A., 2015. Evaluation of dielectric mixing models for passive microwave soil moisture retrieval using data from ComRAD ground-based SMAP simulator. IEEE Journal of Selected Topics in Applied Earth Observations and Remote Sensing 8 (9), 4345–4354. http://dx.doi.org/10.1109/JSTARS.2014.2372031.
Talone, M., Camps, A., Monerris, A., Vall-llossera, M., Ferrazzoli, P., Piles, M., 2007. Surface topography and mixed-pixel effects on the simulated L-band brightness temperatures. IEEE Trans. Geosci. Remote Sens. 45, 1996–2003.
Tian, F., Brandt, M., Liu, Y.Y., Rasmussen, K., Fensholt, R., 2016. Mapping gains and losses in woody vegetation across global tropical drylands. Glob. Chang. Biol. http://dx.doi.org/10.1111/gcb.13464.
Tsang, L., Kong, J.A., Shin, R.T., 1985. Theory of Microwave Remote Sensing. Wiley Interscience Publications, New York.
Ulaby, F., Moore, K., Fung, K., 1986. Microwave Remote Sensing, Active and Passive, Vol. III: From Theory to Applications. Artech House, Massachusettes.
Ulaby, F.T., Wilson, E.A., 1985. Microwave attenuation properties of vegetation canopies. IEEE Trans. Geosci. Remote Sens. GE-23, 746–753.
Utku, C., Le Vine, D.M., 2014. Topographic signatures in aquarius radiometer and scatterometer response. IEEE Trans. Geosci. Remote Sens. 52 (7), 4141–4154.
Van de Griend, A.A., Wigneron, J.P., 2004. The b-factor as a function of frequency and canopy type at H-polarization. IEEE Trans. Geosci. Remote Sens. 42, 786–794.
Van der Schalie, R., Parinussa, R.M., Renzullo, L.J., Van Dijk, A., Su, C.-H., de Jeu, R., 2015. SMOS soil moisture retrievals using the land parameter retrieval model: evaluation over the Murrumbidgee catchment, Southeast Australia. Remote Sens. Environ. 163, 70–79.
Van der Schalie, R., Kerr, Y.H., Wigneron, J.P., Rodríguez-Fernández, N.J., Al-Yaari, A., Jeu, R.A.M.D., 2016. Global SMOS soil moisture retrievals from the land parameter retrieval model. Int. J. Appl. Earth Obs. Geoinf. 45, 125–134. Part P
Vittucci, C., Ferrazzoli, P., Kerr, Y., Richaume, P., Guerriero, L., Rahmoune, R., Laurin, G.V., 2016. SMOS retrieval over forests: exploitation of optical depth and tests of soil moisture estimates. Remote Sens. Environ. 180, 115–127.
Völksch, I., Schwank, M., Stähli, M., Mätzler, C., 2015. Relief effects on the L-band emission of a bare soil. Remote Sens. 7.
Walker, J.P., Houser, P.R., 2001. Initialization of soil moisture in a global climate model: a North American Case Study. EOS Trans. Am. Geophys. Union 82 (47), F457.
Wang, J.R., Choudhury, B.J., 1981. Remote sensing of soil moisture content, over bare field at 1.4 GHz frequency. Journal of Geophysical Research: Oceans 86, 5277–5282.
Wang, J.R., Schmugge, T.J., 1980. An empirical model for the complex dielectric permittivity of soils as a function of water content. Geoscience and Remote Sensing, IEEE Transactions on GE-18, 288–295.
Wang, J.R., O'Neill, P.E., Jackson, T.J., Engman, E.T., 1983. Multifrequency measurements of the effects of soil moisture, soil texture, and surface roughness. Geoscience and Remote Sensing, IEEE Transactions on GE-2
Wang, S., Wigneron, J.P., Jiang, L.M., Parrens, M., Yu, X.Y., Al-Yaari, A., Ye, Q.Y., Fernandez-Moran, R., Ji, W., Kerr, Y., 2015. Global-scale evaluation of roughness effects on C-band AMSR-E observations. Remote Sens. 5734–5757.
Warnick, K.F., Chew, W.C., 2001. Numerical simulation methods for rough surface scattering. Waves in Random Media 11, R1–R3
Wegmüller, U., Matzler, C., 1999. Rough bare soil reflectivity model. IEEE Trans. Geosci. Remote Sens. 37, 1391–1395.
Wiesmann, A., Mätzler, C., 1999. Microwave emission model of layered snowpacks. Remote Sens. Environ. 70, 307–316.
Wigneron, J.-P., Pardé, M., Waldteufel, P., Chanzy, A., Kerr, Y., Schmidl, S., et al., 2004. Characterizing the dependence of vegetation parameters on crop type, view angle and polarization at L-band. IEEE Trans. Geosci. Remote Sens. 42 (2), 416–425.
Wigneron, J.P., Calvet, J.C., Kerr, Y., Chanzy, A., Lopes, A., 1993. Microwave emission of vegetation: sensitivity to leaf characteristics. IEEE Trans. Geosci. Remote Sens. 31, 716–726.
Wigneron, J.P., Waldteufel, P., Chanzy, A., Calvet, J.C., Kerr, Y., 2000. Two-dimensional microwave interferometer retrieval capabilities over land surfaces (SMOS mission). Remote Sens. Environ. 73, 270–282.
Wigneron, J.P., Laguerre, L., Kerr, Y.H., 2001. A simple parameterization of the L-band microwave emission from rough agricultural soils. Geoscience and Remote Sensing, IEEE Transactions on 39, 1697–1707.
Wigneron, J.P., Kerr, Y., Waldteufel, P., Saleh, K., Escorihuela, M.J., Richaume, P., Ferrazzoli, P., de Rosnay, P., Gurney, R., Calvet, J.C., Grant, J.P., Guglielmetti, M., Hornbuckle, B., Mätzler, C., Pellarin, T., Schwank, M., 2007. L-band microwave emission of the biosphere (L-MEB) model: description and calibration against experimental data sets over crop fields. Remote Sens. Environ. 107, 639–655.
Wigneron, J.P., Chanzy, A., De Rosnay, P., Rudiger, C., Calvet, J.C., 2008. Estimating the effective soil temperature at L-band as a function of soil properties. Geoscience and Remote Sensing, IEEE Transactions on 46, 797–807.
Wigneron, J.P., Chanzy, A., Kerr, Y.H., Lawrence, H., Shi, J., Escorihuela, M.J., Mironov, V., Mialon, A., Demontoux, F., Rosnay, P.d., Saleh-Contell, K., 2011. Evaluating an improved parameterization of the soil emission in L-MEB. IEEE Trans. Geosci. Remote Sens. 49, 1177–1189.
Wigneron, J.-P., Chanzy, A., Calvet, J.-C., Bruguier, N., 1995. A simple algorithm to retrieve soil moisture and vegetation biomass using passive microwave measurements over crop fields. Remote Sens. Environ. 51, 331–341.
Wigneron, J.-P., Calvet, J.-C., Kerr, Y., 1996. Monitoring water interception by crop fields from passive microwave observations. Agric. For. Meteorol. 80, 177–194.
Yu, X., Walker, J.P., Rüdiger, C., Panciera, R., Gray, D.A., 2015. Simulation of the SMAP data stream from SMAPEx field campaigns in Australia. IEEE Trans. Geosci. Remote Sens. 53, 1921–1934.
Yan, S., Jiang, L., Chai, L., Yang, J., Kou, X., 2015. Calibration of the L-MEB model for croplands in HiWATER using PLMR observation. Remote Sens. 7.
Zribi, M. & Dechambre, M. (2003). A new empirical model to retrieve soil moisture and roughness from C-band radar data. Remote Sens. Environ., 84, 42–52